when the body was insufficiently lifted. Additionally, when the tail was lifted clear of the media in robot experiments, the posterior motor and mounting structures intruded into and dragged through the media, resulting in an intrusion that was difficult to model; therefore, we simulated trials with the tail intruding into the media in the same configuration as at the end of tail-thrusting behavior, which yielded similar performance. To test these assumptions, we compared results to a subset of robot trials, and obtained good agreement between simulation and experiment (Fig. 4C and fig. S4).

The change in the patterns of the local connection vector fields revealed how limbs and tail could coordinate to produce movement (Fig. 4, C to E). For example, these fields demonstrated that the tail was not uniformly beneficial in all situations, nor even substantially beneficial in horizontal movement, in which the vertical component of the vectors (tail contribution) was small. However, as surface incline angle increased, the horizontal magnitudes of connection vectors decreased, indicating reduced efficacy of limb-only tail-dragging gaits (a horizontal path across the vector field). The relatively larger vertical component across more of the shape space indicated the increased importance of the tail to forward movement. The optimal gait for both inclines was close to the synchronous thrusting used by the robot and mudskipper, yielding similar displacements (Fig. 4, C to E); phase lag between initiation of limb and tail movement was suboptimal and, in one case per incline, yielded the worst possible gait (Fig. 4, D and E). Improper use of the tail resulted in substantially lower performance than simply allowing it to drag (Fig. 4, C to E). Additionally, the generally downward direction of the vectors in both fields demonstrate that purely tail-powered locomotion (a vertical path down the right of the vector field) can produce forward motion, as seen in some extant fish (*12*).

Our results from a biological analog of early tetrapods and robophysical and mathematical models demonstrate that the tail can play an important role in limb-driven crutching locomotion on inclined granular substrates by making locomotors more robust to suboptimal kinematics and substrate conditions. This suggests that the sizable, well-ossified (and presumably well-muscled) tails of early tetrapods (*15*–*17*), originally used for swimming, may have been co-opted to promote reliable locomotion over challenging substrates, providing an exaptation (*36*) that facilitated their invasion of land. Although evidence of tail use is absent among the few fossil trackways attributed to early tetrapods (*37*, *38*), tail use might be evident in trackways formed on inclined shores.

REFERENCES AND NOTES

1. J. A. Clack, *Gaining Ground: The Origin and Evolution of Tetrapods* (Indiana Univ. Press, 2002).
2. E. B. Daeschler, N. H. Shubin, F. A. Jenkins Jr., *Nature* **440**, 757–763 (2006).
3. A. Blieck *et al.*, *Geol. Soc. London Spec. Publ. 278*, 219–235 (2007).
4. N. Gravish, P. B. Umbanhowar, D. I. Goldman, *Phys. Rev. Lett.* **105**, 128301 (2010).
5. H. Marvi *et al.*, *Science* **346**, 224–229 (2014).
6. F. Qian *et al.*, *Bioinspir. Biomim.* **10**, 056014 (2015).
7. C. Li, P. B. Umbanhowar, H. Komsuoglu, D. E. Koditschek, D. I. Goldman, *Proc. Natl. Acad. Sci. U.S.A.* **106**, 3029–3034 (2009).
8. N. Mazouchova, P. B. Umbanhowar, D. I. Goldman, *Bioinspir. Biomim.* **8**, 026007 (2013).
9. J. Davenport, A. K. M. A. Matin, *J. Fish Biol.* **37**, 175–184 (1990).
10. A. G. Johnels, *Oikos* **8**, 122 (1957).
11. C. M. Pace, A. C. Gibb, *J. Exp. Biol.* **214**, 530–537 (2011).
12. C. M. Pace, A. C. Gibb, *J. Fish Biol.* **84**, 639–660 (2014).
13. A. Jusufi, D. I. Goldman, S. Revzen, R. J. Full, *Proc. Natl. Acad. Sci. U.S.A.* **105**, 4215–4219 (2008).
14. T. Libby *et al.*, *Nature* **481**, 181–184 (2012).
15. E. Jarvik, *Medd. Gronl.* **114**, 1–90 (1952).
16. E. Jarvik, *The Devonian Tetrapod* Ichthyostega (Indiana Univ. Press, 1996).
17. M. I. Coates, *Trans. R. Soc. Edinb. Earth Sci.* **87**, 363–421 (1996).
18. R. W. Blob, *Paleobiology* **27**, 14–38 (2001).
19. M. A. Ashley-Ross, S. T. Hsieh, A. C. Gibb, R. W. Blob, *Integr. Comp. Biol.* **53**, 192–196 (2013).
20. S. E. Pierce, J. A. Clack, J. R. Hutchinson, *Nature* **486**, 523–526 (2012).
21. S. E. Pierce, J. R. Hutchinson, J. A. Clack, *Integr. Comp. Biol.* **53**, 209–223 (2013).
22. E. M. Standen, T. Y. Du, H. C. E. Larsson, *Nature* **513**, 54–58 (2014).
23. S. M. Kawano, R. W. Blob, *Integr. Comp. Biol.* **53**, 283–294 (2013).
24. V. A. Harris, *Proc. Zool. Soc. London* **134**, 107–135 (1960).
25. B. O. Swanson, A. C. Gibb, *J. Exp. Biol.* **207**, 4037–4044 (2004).
26. J. Aguilar, D. I. Goldman, *Nat. Phys.* **12**, 278 (2016).
27. A. Shapere, F. Wilczek, *Phys. Rev. Lett.* **58**, 2051–2054 (1987).
28. R. L. Hatton, Y. Ding, H. Choset, D. I. Goldman, *Phys. Rev. Lett.* **110**, 078101 (2013).
29. N. Mitarai, F. Nori, *Adv. Phys.* **55**, 1–45 (2006).
30. S. S. Sharpe, R. Kuckuk, D. I. Goldman, *Phys. Biol.* **12**, 046009 (2015).
31. H. Askari, K. Kamrin, http://arxiv.org/abs/1510.02966 (2015).
32. K. Nishikawa *et al.*, *Integr. Comp. Biol.* **47**, 16–54 (2007).
33. C. Li, T. Zhang, D. I. Goldman, *Science* **339**, 1408–1412 (2013).
34. S. D. Kelly, R. M. Murray, *J. Robot. Syst.* **12**, 417–431 (1995).
35. R. D. Maladen, Y. Ding, C. Li, D. I. Goldman, *Science* **325**, 314–318 (2009).
36. S. J. Gould, E. S. Vrba, *Paleobiology* **8**, 4–15 (1982).
37. J. Clack, *Palaeogeogr. Palaeoclimatol. Palaeoecol.* **130**, 227–250 (1997).
38. S. Curth, M. S. Fischer, J. A. Nyakatura, *Ichnos* **21**, 32–43 (2014).

ACKNOWLEDGMENTS

Supported by NSF grants PoLS PHY-1205878, PHY-1150760, and CMMI-1361778, Army Research Office (ARO) grant W911NF-11-1-0514, and the ARL MAST CTA (D.I.G.); ARO Robotics CTA and NSF National Robotics Initiative IIS-1426655 (H.C.); NSF grants IOS-0517340 and IOS-0817794 (R.W.B.); GT UROP and the GT PURA Travel Grant (B.M.); a Clemson University Wade Stackhouse Fellowship, NSF award DBI-1300426, and the University of Tennessee, Knoxville (S.M.K.); and the U.S. Department of Defense, Air Force Office of Scientific Research, National Defense Science and Engineering Graduate (NDSEG) Fellowship, 32 CFR 168a (P.E.S.). The authors declare no conflicts of interest. Data are available from the corresponding author upon request.

SUPPLEMENTARY MATERIALS

www.sciencemag.org/content/353/6295/154/suppl/DC1
Materials and Methods
Supplementary Text
Figs. S1 to S6
Table S1
Movies S1 to S6
References (*39*, *40*)

16 December 2015; accepted 26 May 2016
10.1126/science.aaf0984

ROBOTICS

Phototactic guidance of a tissue-engineered soft-robotic ray

Sung-Jin Park,[1] Mattia Gazzola,[2]* Kyung Soo Park,[3,4]† Shirley Park,[5]‡ Valentina Di Santo,[6] Erin L. Blevins,[6]§ Johan U. Lind,[1] Patrick H. Campbell,[1] Stephanie Dauth,[1] Andrew K. Capulli,[1] Francesco S. Pasqualini,[1] Seungkuk Ahn,[1] Alexander Cho,[1] Hongyan Yuan,[1]|| Ben M. Maoz,[1] Ragu Vijaykumar,[5] Jeong-Woo Choi,[3,4] Karl Deisseroth,[5,7] George V. Lauder,[6] L. Mahadevan,[2,8] Kevin Kit Parker[1,4]¶

Inspired by the relatively simple morphological blueprint provided by batoid fish such as stingrays and skates, we created a biohybrid system that enables an artificial animal—a tissue-engineered ray—to swim and phototactically follow a light cue. By patterning dissociated rat cardiomyocytes on an elastomeric body enclosing a microfabricated gold skeleton, we replicated fish morphology at $^{1}/_{10}$ scale and captured basic fin deflection patterns of batoid fish. Optogenetics allows for phototactic guidance, steering, and turning maneuvers. Optical stimulation induced sequential muscle activation via serpentine-patterned muscle circuits, leading to coordinated undulatory swimming. The speed and direction of the ray was controlled by modulating light frequency and by independently eliciting right and left fins, allowing the biohybrid machine to maneuver through an obstacle course.

Bioinspired design, as applied to robotics, aims at implementing naturally occurring features such as soft materials, morphologies, gaits, and control mechanisms in artificial settings in order to improve performance (*1*–*4*). For example, recent soft-robotics studies raised awareness on the importance of material properties (*3*, *4*), shifting the focus from rigid elements to soft materials, whereas other investigations report successful mimicry of gaits or morphological features inspired by insects (*5*, *6*), fish (*7*, *8*), snakes (*9*), salamanders (*10*), and cheetahs (*11*). Although recent advances have the promise of bridging the performance gap with animals,

the current soft-robotic actuators based on, for instance, electroactive polymers, shape memory alloys, or pressurized fluids are yet to mature to the point of replicating the high-resolution complex movements of biological muscles (*3*, *4*).

In this context, biosensors and bioactuators (*12*) are intriguing alternatives because they can intrinsically respond to a number of control inputs (such as electric fields and optical stimulation). Thanks to recent advances in genetic tools (*13*) and tissue engineering (*12*), these responses can be altered and tuned across a wide range of time and length scales. Some pioneering studies have exploited these technologies for self-propulsion, developing miniaturized walking machines (*14*–*16*) and flagellar (*17*) or jellyfish-inspired (*18*) swimming devices. These biohybrid systems operate at high energy efficiency and harvest power from energy-dense, locally available nutrients, although at present they require specialized environments (physiological solutions) that may limit their applicability. Moreover, these biohybrid locomotors lack the reflexive control (*9*, *19*) necessary to enable adaptive maneuvering and thus the ability to respond to spatiotemporally varying external stimuli.

We designed, built, and tested a tissue-engineered analog of a batoid fish such as stingrays and skates. By combining soft materials and tissue engineering with optogenetics, we created an integrated sensory-motor system that allowed for coordinated undulating fin movement and phototactically controlled locomotion that is guided via light stimuli. We drew from fish morphology, neuromuscular dynamics, and gait control to implement a living, biohybrid system that leads to robust and reproducible locomotion and turning maneuvers. Batoid fish are ideal biological models in robotics (*8*) because their nearly planar bauplan is characterized by a broad dorsoventral disk, with a flattened body and extended pectoral fins, that enhances stability against roll (*20*). They swim with high energy efficiency (*21*) by generating spanwise bending deformations and chordwise front-to-rear undulatory motion (Fig. 1A and movie S1) (*20*, *22*) via the sequential activation of pectoral fin muscles. This undulatory gait allows slender aquatic animals to channel body movement into forward motion by exchanging momentum with the fluid (*7*, *22*) and is a convergent mode of aquatic propulsion (*23*). Moreover, batoids can use these undulatory modes for fine maneuvering and turning by independently and asymmetrically actuating their pectoral fins (*24*). Inspired by batoids, we reverse-engineered their musculoskeletal structure (Fig. 1B and fig. S1) via a four-layered architecture (Fig. 1C): a three-dimensional elastomer [polydimethylsiloxane (PDMS)] body, cast via a titanium mold (fig. S2A and movie S2); a chemically neutral skeleton fabricated by means of thermal evaporation of gold through a custom designed shadow mask; a thin interstitial elastomer layer obtained by spin-coating; and last, a layer of aligned rat cardiomyocytes generated via microcontact printing of fibronectin (fig. S3) (*25*).

This design yielded a tissue-engineered ray with a single muscle layer capable of downward contraction (Fig. 1, C and D). Upward contraction would require a second layer of muscle that acts antagonistically to the upper layer. To minimize the complexity of our design, we instead used an asymmetrical stiff gold skeleton that stores elastic energy during the downstroke and rebounds during the subsequent relaxation phase. Inspired by histological analysis (fig. S1) as well as theoretical considerations (*26*), we channeled muscular work and elastic energy into forward motion by breaking fore-aft symmetry through a varying body rigidity along the anterior-posterior axis. This was achieved via a thicker body and a denser and radially further reaching skeleton pattern in the front (Figs. 1, C and D, and 2A and fig. S2A). Likewise, along the proximal-distal axis, flexibility of the fins was enhanced by gradually reducing their thickness (fig. S2A). Last, the PDMS mixture was adjusted (*25*) to provide body rigidity and fin flexibility while conserving overall neutral buoyancy (fig. S2).

The composite supporting structure described above was coupled to a tissue-engineered muscle layer, which captured the salient musculoskeletal features of batoid fish (Fig. 2B). At the mesoscale (50 μm to 5 mm), batoid myofibers are tightly bundled and are aligned in the radial direction parallel to the rays of the skeleton (Fig. 2B). At the microscale (1 to 10 μm), the Z-lines of the sarcomeres (the cell force–generating units) (Fig. 2C) present strong nematic alignment perpendicular to individual myofibers so as to focus contraction forces. Following this layout, the muscles and sarcomeres of the tissue-engineered ray were designed to orient radially from the body and parallel to the gold skeleton rays (Fig. 2B and fig. S4), and the Z-lines of the sarcomeres were engineered to be perpendicular to the skeleton rays through microscale patterning of fibronectin (Fig. 2C and fig. S4).

Last, to mimic the sensory-somatic nervous system that controls the sequential activation of fin muscles in the batoid fish, we recast the neurocontrol problem as a design problem. A possible solution is given by serpentine-patterned muscle circuits that physically determine the propagation of muscle contraction in space and time (Figs. 1D and 2, D and E), leading to hardwired coordination that could be triggered with external

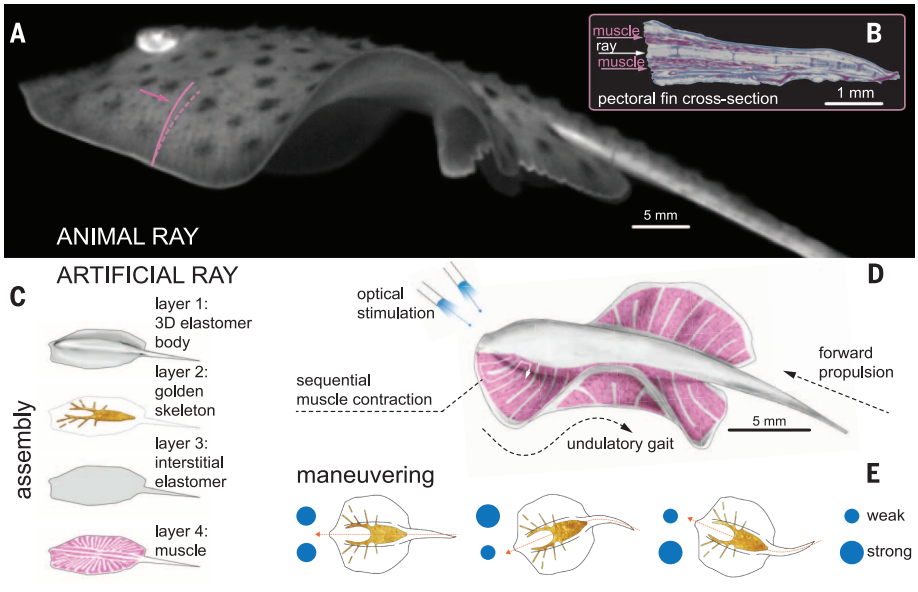

Fig. 1. Bioinspired concept design of the tissue-engineered ray. (**A**) A live Little skate, *Leucoraja erinacea*, swimming and (**B**) its musculoskeletal structure. (**C** to **E**) Tissue-engineered ray with (C) four layers of body architecture, (D) concept, and (E) phototactic control. Upon optical stimulation, the tissue-engineered ray induces sequential muscle activation via serpentine-patterned muscle tissues, generates undulatory locomotion, and sustains steady forward swimming. It changes direction by generating asymmetric undulating motion between left and right fins, modulated by light pulse frequency.

[1]Disease Biophysics Group, Wyss Institute for Biologically Inspired Engineering, John A. Paulson School of Engineering and Applied Sciences, Harvard University, Cambridge, MA 02138, USA. [2]John A. Paulson School of Engineering and Applied Sciences, Harvard University, Cambridge, MA 02138, USA. [3]Department of Chemical and Biomolecular Engineering, Sogang University, Seoul 121-742, Korea. [4]Sogang-Harvard Research Center for Disease Biophysics, Sogang University, Seoul 121-742, Korea. [5]Department of Bioengineering, Stanford University, Stanford, CA 94305, USA. [6]Museum of Comparative Zoology, Harvard University, Cambridge, MA 02138, USA. [7]Department of Psychiatry and Behavioral Sciences and the Howard Hughes Medical Institute, Stanford University, Stanford, CA 94305, USA. [8]Department of Organismic and Evolutionary Biology, Department of Physics, Wyss Institute for Biologically Inspired Engineering, Kavli Institute for Nanobio Science and Technology, Harvard University, Cambridge, MA 02138S, USA.
*Present address: Department of Mechanical Science and Engineering, University of Illinois at Urbana-Champaign, Urbana, IL 61801, USA. †Present address: Department of Biomedical Engineering, University of Michigan, Ann Arbor, MI 48109, USA. ‡Present address: Department of Cardiovascular Medicine, Stanford University Medical Center, Stanford, CA 94305, USA. §Present address: The Winsor School, Boston, MA 02215, USA. ||Present address: Department of Mechanical, Industrial and Systems Engineering, University of Rhode Island, Kingston, RI 02881, USA.
¶Corresponding author. Email: kkparker@seas.harvard.edu

stimuli. This design was implemented by overlaying onto anisotropic tissue a layer of cardiomyocytes that were electrically coupled with gap junctions (fig. S4H). These myocytes were engineered to respond to optical stimuli (Fig. 1D) by expressing a light-sensitive ion channel [channelrhodopsin-2 (ChR2)] (*27*). Thus, a point light stimulus directed at the front of the ray triggers the propagation of an action potential that is spatially and temporally modulated by the gap junctions between muscle cells without the need for neural coupling and coordination (Fig. 2, D and E). The expression of ChR2 was obtained via lentiviral transduction mediated by the truncated cardiac troponin T promoter cTnT (fig. S5) (*25*, *28*). This approach led to an 88% transduction rate of cardiomyocytes and maximized the sensitivity to blue light at powers of ~10 mW (fig. S5).

Optical stimulation of the circuits initiated sequential activation waves that propagated along the anterior-posterior axis as revealed by means of calcium imaging (*25*) for three different circuit designs (Fig. 2D, fig. S6, and movies S3 and S4). Dense serpentine patterns enhanced activation localization, whereas rarefied ones increased propagation speed (figs. S7 and S8). To allow for maneuverability, we ensured that each pectoral fin could be independently actuated by pacing left and right optical stimuli at different frequencies (fig. S6 and movie S5). Among the various designs considered, the circuit of choice was characterized by the intermediate serpentine pattern density (Fig. 2E). This circuit represented the best tradeoff between overlap with batoids' operating range and contraction time reproducibility (low standard error) in order to minimize desynchronization and undesired turning (Fig. 2E). The final overall design of our ray consists of ~200,000 live cardiomyocytes in an elastomeric body of 16.3 mm length and 10.18 ± 0.43 mg mass.

When immersed in a 37°C Tyrode's physiological salt solution containing glucose as energy reservoir, and upon optical stimulation, the fabricated ray was propelled by producing forward thrust via the undulatory motion of its fins (Fig. 3 and movie S6). Video-tracking analysis (*25*) showed that during each swimming cycle, as the calcium signal propagated (fig. S9), the anterior region bent downward, while the posterior one lifted upward (Fig. 3, A and B), conferring a small downward orientation (–10°) to the ray's longitudinal axis (fig. S9). Both regions reached their maximum displacement around ~200 ms (Fig. 3B), when their motion gradually inverted until ~340 ms

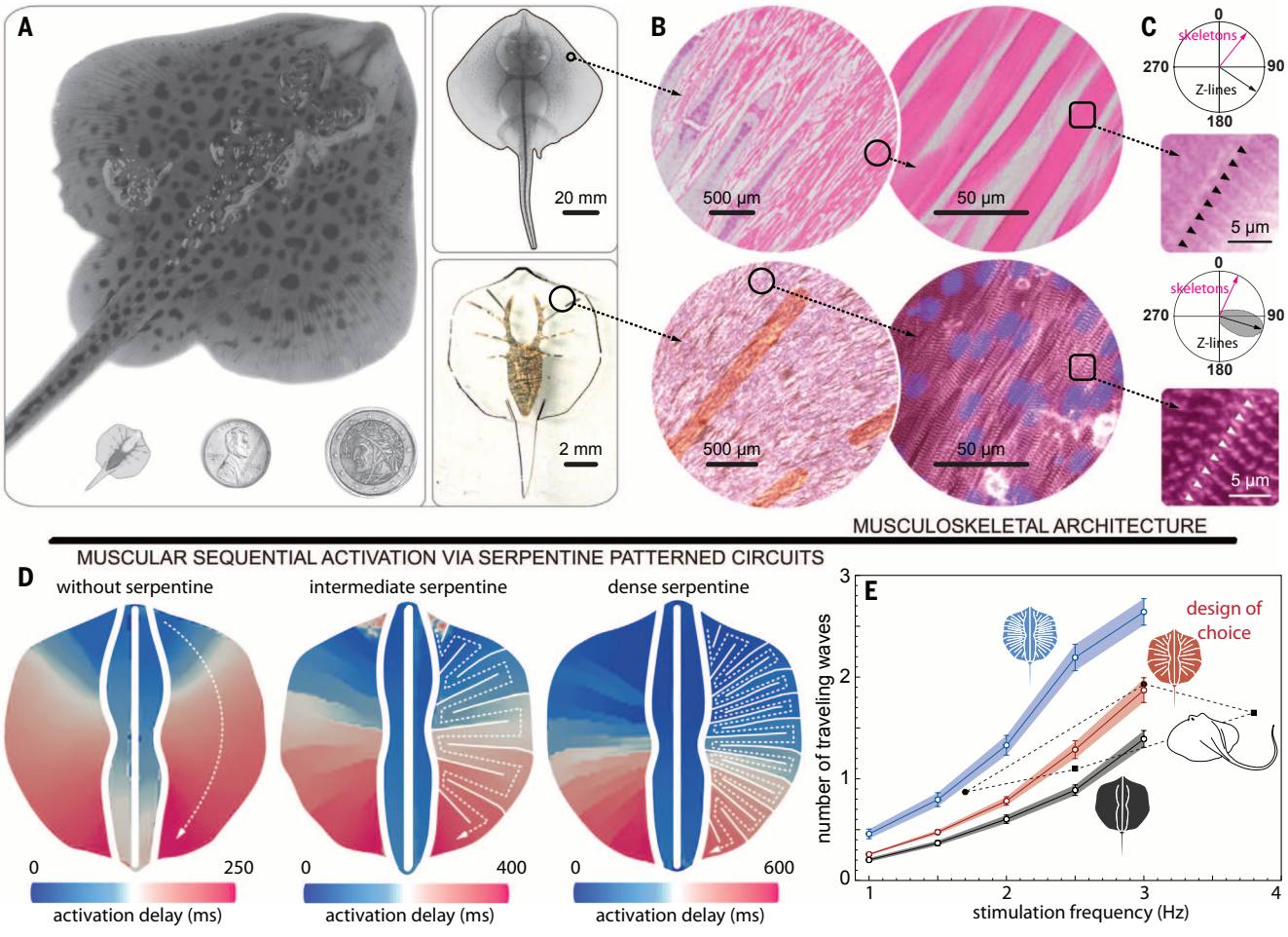

Fig. 2. Engineering solutions. (**A**) System-level design for skate (top) and tissue-engineered ray (bottom left) comparable with one penny and a two Euros coin (bottom middle and right). (**B** and **C**) Musculoskeletal (B) meso- and (C) micro-architecture of a skate, *L. erinacea* (top), is replicated in a tissue-engineered ray (bottom). Horizontal sections of the skate were stained with hematoxylin and eosin (top), and the engineered tissue was immunostained with a light-sensitive membrane protein, ChR2 (red, bottom left), sarcomeric α-actinin [red, (B), bottom right, and (C)], and nuclei (blue, (B), bottom right). (C) Orientation of the Z-lines (skate, black arrow and black triangles, top; and tissue-engineered ray, black arrow with gray distribution and white triangles, bottom). In both cases, Z-lines are perpendicular to the skeleton rays (pink arrows). (**D**) Muscle circuits with preprogrammed activation pattern. A point light stimulus directed at the front of the fins with 1.5 Hz frequency triggers the calcium wave that propagates along the predefined serpentine patterns. (**E**) Operating range of the muscle circuits. The circuit with intermediate serpentine pattern density represents the best tradeoff between contraction time reproducibility (SEM) and overlap with batoids' operating range [*Taeniura lymma* (*20*) and *Potamotrygon orbignyi* (*22*), black symbols]. Black, red, and blue indicates muscle circuit without serpentine patterns and with intermediate and dense serpentine patterns, respectively. Each colored band indicates SEM of number of traveling waves.

(Fig. 3, C and D). At this point, the calcium wave had traveled ~70% of the ray body and approached the flexible tail region (Fig. 3E and fig. S9). This signal caused a rapid, strong downward contraction of the rear of the body, a quick upward recoil of the head region (presumably mediated by the stiff skeleton) (Fig. 3), a 30° upward reorientation of the longitudinal axis (fig. S9), and a spike in forward swimming speed (Fig. 3E). After 340 ms, the calcium wave vanishes, and the ray relaxes (Fig. 3E and fig. S9), gliding until its forward momentum dissipates.

A periodical optical stimulation leads to a rhythmically sustained forward displacement (Fig. 3F). To test the benefits of spatiotemporally modulated undulatory locomotion relative to pulsatile locomotion (typical of jellyfish), we stimulated our design of choice via a global electrical field (*25*). The latter, unlike optical point stimulation, induces a global, synchronized contraction of the entire muscle layer, leading to jet-like propulsion (movie S7). Although pulsatile actuation also produced forward motion, undulatory gaits were found to be twice as fast at 1.5 Hz pacing (Fig. 3G).

We compared the kinematics (Fig. 3, H and I) and hydrodynamics (Fig. 3, J to M) of bioinspired and live rays. Both rays exhibit asymmetric deformation patterns in which the deflection amplitude progressively increases in the radially outward and anterior-posterior directions. This similarity shows that our asymmetric composite structure compensates for the lack of the upper muscle layer (Fig. 3, B and D), leading to the coordinated undulatory locomotion. Our design of choice was found to outperform a symmetric design (by 5.7×, as measured by distance traveled per unit time) as well as asymmetric designs without gold skeleton (2.7×), with denser gold skeleton (8.2×), and with thinner (1.5×) and thicker fins (3.3×) (fig. S10 and movie S8 and S9). Particle image velocimetry (PIV) (*25*) images of the hydrodynamic footprint of the tissue-engineered ray (Fig. 3, A to D) show that body contractions generate vortices of alternating sign that are sequentially shed downstream in the wake (Fig. 3, A to D, and movie S10), which is the hallmark of inertial undulatory swimming (*29*). Indeed, PIV of live skates (Fig. 3, K to M, and fig. S11) reveals a qualitatively similar alternation of positive and negative vortices, respectively generated in concave and convex regions of the body.

We emphasize here that our ray is a 10-fold scaled-down version of a live skate and moves in a laminar flow regime, as opposed to batoid fish that operate in turbulent conditions. Thus, a direct performance comparison is not meaningful, but it is instructive to contextualize artificial and natural solutions in terms of a recent scaling framework (*23*, *30*). All inertial undulatory swimmers hew to two scaling laws, $Re = Sw^{4/3}$ in the laminar regime and $Re = Sw$ in the turbulent regime, where the Swimming number $Sw = 2\pi fAL/\upsilon$ (L is the characteristic length of the swimmer, f is the undulation frequency, A is the amplitude, and υ is the fluid viscosity) captures input kinematics, and the Reynolds number $Re = UL/\upsilon$ (where U is the forward speed) captures output speed. By fitting extant biological data (*23*), the average swimming "roofline" was determined, thus providing an objective way to assess swimming performance. In this analysis, our tissue-engineered rays reached up to 63% of the Re of comparable natural solutions at the given Sw (Fig. 3J).

For gait control, we first determined a set of gait protocols for speed and direction control by modulating light frequency and by synchronously or asynchronously triggering the right and left serpentine circuits (figs. S11 and S12 and movies S12 to S18). Synchronous pacing on both fins resulted in straight, forward displacement (figs. S11 and S12 and movies S12 and S13), whereas stimulation frequency determined the swimming speed range (maximum at 1.5 to 2 Hz, minimum at 1 or 3 Hz) (fig. S10E and movies S14 to S16). Asynchronous pacing instead resulted in directional

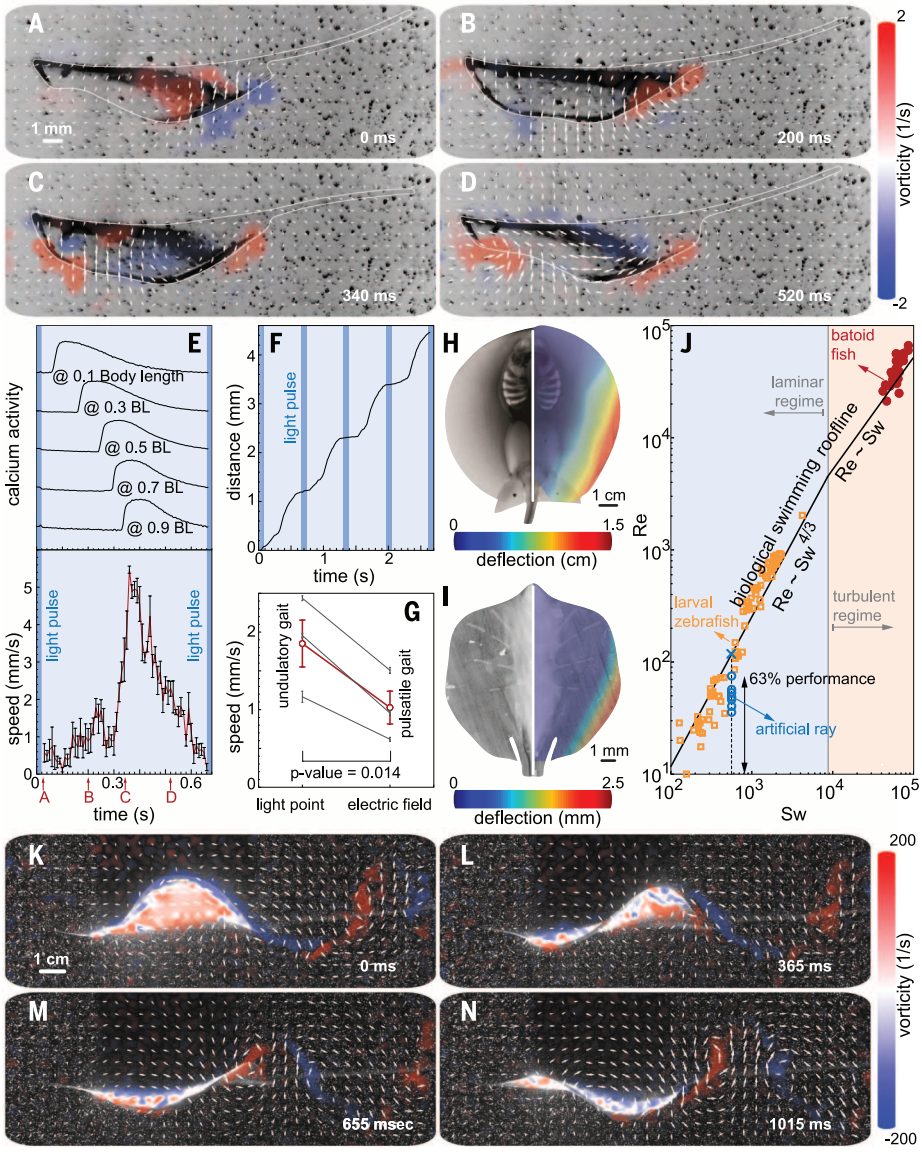

Fig. 3. Kinematics and hydrodynamics. (**A** to **D**) PIV flow measurements highlight the production of alternated positive and negative vortices by the tissue-engineered ray. The viscosity associated with the relatively small *Re* is responsible for the dissipation of the vortex street in the wake. (**E**) Correlation between calcium activity and undulatory locomotion. (**F**) The moving distance during four strokes. (**G**) Comparison of swimming speed between the tissue-engineered rays stimulated by point and field stimulations. Undulatory locomotion produced by sequential muscle activation (point, 1.85 mm/s) improved swimming speed significantly compared with pulsatile propulsion generated by global muscle activation (field, 1.03 mm/s; matched pairs test, $P = 0.014$, $n = 3$ rays). Gray and red lines indicate the speed of individual rays and their average, respectively. (**H** and **I**) Out-of-plane fin deflection in both (H) a live stingray, *P. orbignyi*, and (I) a tissue-engineered ray (maximum amplitude, 2.54 ± 0.02 mm). (**J**) Comparison of swimming performance between tissue-engineered rays ($n = 7$ rays) and aquatic swimmers [batoid fish (*20*) and larval zebrafish (*32*)] following the scaling analysis (*23*). [Figure adapted from (*23*).] (**K** to **N**) PIV analysis of live Little skate, *L. erinacea*.

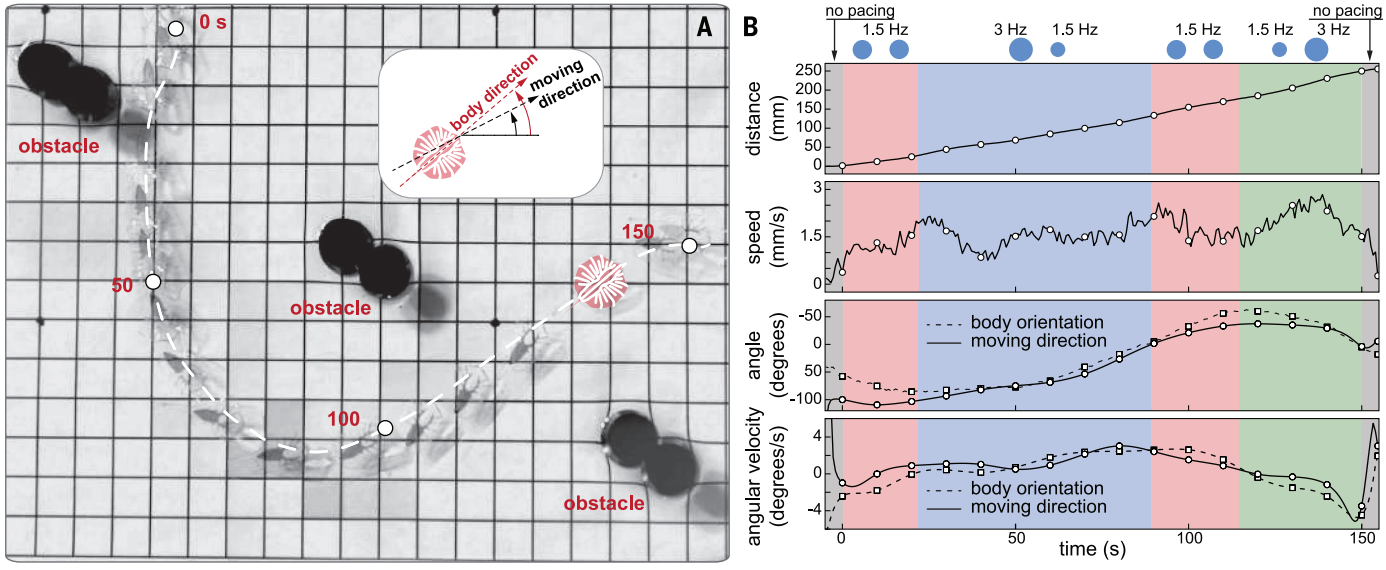

Fig. 4. Phototactic steering of the tissue-engineered ray through an obstacle course. (**A**) The ray completed a course that required complex coordination and maneuvering. Motion began with a forward protocol (at 0 s) to gain acceleration. A following left turn protocol allowed the ray to overcome forward momentum, making a left turn (at ~50 s). Next, another forward protocol was used to dissipate counterclockwise angular momentum and regain directionality (at ~100 s). While the ray made its way back to the other side of the obstacles, a final right turn protocol was given to make a right turn, winding the last obstacle. Grids, 1 cm. (**B**) Corresponding kinematic analysis relative to light frequency modulation protocols used for guidance.

turns (fig. S12, B, C, and F). In order to minimize the turning radius, we paired stimulation frequencies (1/1.5 Hz in movie S17, or 3/1.5 Hz in movie S18) to maximize the actuation difference between fins. Our ray turned in either clockwise or counterclockwise directions by generating asymmetric undulating motion between left and right fins, as in batoid fishes (*24*).

Last, we challenged the tissue-engineered ray to swim through an obstacle course. Using the above gait and turning protocols, we guided the ray along a curved path by alternating forward motion and turning maneuvers, at an average speed of ~1.5 mm/s over a distance of ~250 mm, 15 times longer than its body length (Fig. 4 and movie S19). Furthermore, the ray was found able to maintain 80% of its initial speed for up to 6 consecutive days (fig. S13 and movie S20). Therefore, our ray outperformed existing locomotive biohybrid systems in terms of speed [3.2 mm/s in movie S16, 1.3× over jellyfish (*18*)], distance traveled [~250 mm, 35× over cantilever-like walkers (*15*)], and durability (6 days), demonstrating the potential of self-propelled, phototactically activated tissue-engineered robots.

With dissociated cells, naturally equipped with biosensors and bioactuators, as a programmable, actuating building material, we used optogenetics and tissue engineering to build an adaptive swimming animal. Our study is but a first step in engineering multilevel systems that link neurodynamics, mechanics, and complex controllable gaits—coupling sensory information to motor coordination and movement that leads to behavior. This work paves the way for the development of autonomous and adaptive artificial creatures able to process multiple sensory inputs and produce complex behaviors in distributed systems and may represent a path toward soft-robotic "embodied cognition" (*4*, *31*).

REFERENCES AND NOTES

1. R. Pfeifer, M. Lungarella, F. Iida, *Science* **318**, 1088–1093 (2007).
2. M. Haberland, S. Kim, *Bioinspir. Biomim.* **10**, 016010 (2015).
3. S. Kim, C. Laschi, B. Trimmer, *Trends Biotechnol.* **31**, 287–294 (2013).
4. D. Rus, M. T. Tolley, *Nature* **521**, 467–475 (2015).
5. K. Y. Ma, P. Chirarattananon, S. B. Fuller, R. J. Wood, *Science* **340**, 603–607 (2013).
6. J. S. Koh *et al.*, *Science* **349**, 517–521 (2015).
7. M. S. Triantafyllou, G. S. Triantafyllou, *Sci. Am.* **272**, 64–70 (1995).
8. K. W. Moored, F. E. Fish, T. H. Kemp, H. Bart-Smith, *Mar. Technol. Soc. J.* **45**, 99–109 (2011).
9. H. C. Astley *et al.*, *Proc. Natl. Acad. Sci. U.S.A.* **112**, 6200–6205 (2015).
10. A. J. Ijspeert, A. Crespi, D. Ryczko, J. M. Cabelguen, *Science* **315**, 1416–1420 (2007).
11. D. J. Hyun, S. Seok, J. Lee, S. Kim, *Int. J. Robot. Res.* **33**, 1417–1445 (2014).
12. V. Chan, H. H. Asada, R. Bashir, *Lab Chip* **14**, 653–670 (2014).
13. J. D. Sander, J. K. Joung, *Nat. Biotechnol.* **32**, 347–355 (2014).
14. A. W. Feinberg *et al.*, *Science* **317**, 1366–1370 (2007).
15. V. Chan *et al.*, *Sci Rep* **2**, 857 (2012).
16. R. Raman *et al.*, *Proc. Natl. Acad. Sci. U.S.A.* **113**, 3497–3502 (2016).
17. B. J. Williams, S. V. Anand, J. Rajagopalan, M. T. A. Saif, *Nat. Commun.* **5**, 3081 (2014).
18. J. C. Nawroth *et al.*, *Nat. Biotechnol.* **30**, 792–797 (2012).
19. V. Braitenberg, *Vehicles: Experiments in Synthetic Psychology* (MIT Press, 1986).
20. L. J. Rosenberger, M. W. Westneat, *J. Exp. Biol.* **202**, 3523–3539 (1999).
21. V. Di Santo, C. P. Kenaley, *J. Exp. Biol.* **219**, 1804–1807 (2016).
22. E. L. Blevins, G. V. Lauder, *J. Exp. Biol.* **215**, 3231–3241 (2012).
23. M. Gazzola, M. Argentina, L. Mahadevan, *Nat. Phys.* **10**, 758–761 (2014).
24. J. M. Parson, F. E. Fish, A. J. Nicastro, *J. Exp. Mar. Biol. Ecol.* **402**, 12–18 (2011).
25. Materials and methods are available as supplementary materials on *Science* Online.
26. M. Gazzola, M. Argentina, L. Mahadevan, *Proc. Natl. Acad. Sci. U.S.A.* **112**, 3874–3879 (2015).
27. E. S. Boyden, F. Zhang, E. Bamberg, G. Nagel, K. Deisseroth, *Nat. Neurosci.* **8**, 1263–1268 (2005).
28. H. Ma, C. M. Sumbilla, I. K. G. Farrance, M. G. Klein, G. Inesi, *Am. J. Physiol. Cell Physiol.* **286**, C556–C564 (2004).
29. W. M. van Rees, M. Gazzola, P. Koumoutsakos, *J. Fluid Mech.* **722**, R3 (2013).
30. A. J. Cote, P. W. Webb, *Integr. Comp. Biol.* **55**, 662–672 (2015).
31. R. Pfeifer, H. G. Marques, F. Iida, Soft robotics: The next generation of intelligent machines. *Proceedings of the Twenty-Third International Joint Conference on Artificial Intelligence*, 3–9 August 2013, Beijing, China, pp. 5–11 (2013).
32. U. K. Müller, J. L. van Leeuwen, *J. Exp. Biol.* **207**, 853–868 (2004).

ACKNOWLEDGMENTS

Data reported in the paper are included in the supplementary materials. We thank A. P. Nesmith, M. McKenna, and A. Chandler for discussion on design and K. Hudson and Margherita Gazzola for photography and illustrations. This work was funded by the Harvard Paulson School of Engineering and Applied Sciences, the Wyss Institute for Biologically Inspired Engineering, the National Center for Advancing Translational Sciences grant UH3TR000522, subcontract 312659 from Los Almos National Laboratory under prime DTRA contract DE-AC52-06NA25396, the National Science Foundation (NSF) grant EFRI-0938043, NSF Materials Research Science and Engineering Center grant DMR-1420570, Office of Naval Research Multidisciplinary University Research Initiative grant N000141410533, the Swiss National Science Foundation, the MacArthur Foundation, the Radcliffe Institute, the National Research Foundation of Korea grant 2013K1A4A3055268, and the U.S. Army Research Laboratory and Office contract W911NF-12-2-0036. The views and conclusions contained in this Report are those of the authors and should not be interpreted as representing official policies, expressed or implied, of the Army Research Office or Laboratory, the U.S. government, or any other funding agencies. The U.S. government is authorized to reproduce and distribute reprints for government purposes notwithstanding any copyright notation hereon. Portions of this work were performed at the Harvard Center for Nanoscale Systems (NSF 1541959) and at the Neurobiology Imaging Facility (NINDS P30 Core Center NS072030). Certain aspects of the paper are described in U.S. patent 8,492,150 and U.S. patent application 20150182679.

SUPPLEMENTARY MATERIALS

www.sciencemag.org/content/353/6295/158/suppl/DC1
Materials and Methods
Supplementary Text
Figs. S1 to S15
References (*33*–*44*)
Movies S1 to S20

6 February 2016; accepted 19 May 2016
10.1126/science.aaf4292

Editor's Summary

Swim into the light

A bio-inspired swimming robot that mimics a ray fish can be guided by light. Park *et al*. built a 1/10th-scale version of a ray fish with a microfabricated gold skeleton and a rubber body powered by rat heart muscle cells. The cardiomyocytes were genetically engineered to respond to light cues, so that the undulatory movements propelling the robot through water would follow a light source.

Science, this issue p. 158

www.sciencemag.org/content/353/6295/158/suppl/DC1

Supplementary Material for

Phototactic guidance of a tissue-engineered soft-robotic ray

Sung-Jin Park, Mattia Gazzola, Kyung Soo Park, Shirley Park, Valentina Di Santo, Erin L. Blevins, Johan U. Lind, Patrick H. Campbell, Stephanie Dauth, Andrew K. Capulli, Francesco S. Pasqualini, Seungkuk Ahn, Alexander Cho, Hongyan Yuan, Ben M. Maoz, Ragu Vijaykumar, Jeong-Woo Choi, Karl Deisseroth, George V. Lauder, L. Mahadevan, Kevin Kit Parker*

*Corresponding author. Email: kkparker@seas.harvard.edu

Published 8 July 2016, *Science* **353**, 158 (2016)
DOI: 10.1126/science.aaf4292

This PDF file includes:

Other Supplementary Material for this manuscript includes the following:
(available at www.sciencemag.org/content/353/6295/158/suppl/DC1)

Movies S1 to S20

Materials and Methods

Animal batoid histology preparation

All animal procedures were done in accordance with the guidelines of Harvard University's Animal Care and Use Committee. The juvenile batoid fish, Little Skates (*Leucoraja erinacea*), were purchased from a local collector as egg cases and were allowed to develop and hatch in the laboratory. Tissue samples were collected from those that died naturally, and frozen for storage. Tissue samples of *L. erinacea* were thawed and fixed in 4% Paraformaldehyde (SigmaAldrich, St. Louis, MO), which were incubated at 4ºC for 24 hours. The samples were decalcificated with 1.35 M HCl Cal-EX (Fisher scientific, Pittsburgh, PA) for 75 mins and rinsed with PBS before and after decalcification. Paraffin embedding, sectioning, and staining with hematoxylin and eosin and Mallory's trichrome were completed by Ricasan Rowley Histology Consulting, Danvers, MA.

Neonatal Ventricular Myocyte Harvest

The neonatal ventricular myocyte isolation procedure was performed as previously described (*14*). Briefly, ventricles were removed from 2 day old Sprague Dawley rat pups (Charles River Laboratories, Wilmington, MA) and the tissue was manually minced and placed in a 0.1% trypsin (SigmaAldrich, St. Louis, MO) at 4ºC for approximately 12 hours of enzymatic digestion with gentle rocker agitation. The trypsin was then removed and replaced with 0.1% type II collagenase (SigmaAldrich, St. Louis, MO) for a second stage of enzymatic digestion. After four serial digestions at 37 ºC, ventricular myocytes were further isolated from the resulting dissociated cell solution by two centrifugations, between which cells were passed through a 40 µm cell strainer and finally two 45 minute pre-plates at 37 ºC. Fibroblasts remaining from the pre-plates were retained and stored in an incubator to be used as a control for cardiac specific expression of ChR2. The resulting isolated ventricular myocytes were then resuspended in a supplemented M199 cell media (Invitrogen, Carlsbad, CA) with 10% heat-activated fetal bovine serum (FBS) (Invitrogen, Carlsbad, CA) to create the seeding solution.

Tissue-engineered ray fabrication

The fabrication process of the tissue-engineered ray (fig. S3) was developed by modifying the processes to build muscular thin films (*14, 33*) and the tissue-engineered jellyfish (*18*). First, titanium (Ti) molds were designed by a computer-aided design tool, Solidworks (Waltham, MA), and fabricated by milling and polishing a 500-µm deep cavity in the Machine Shop / 3D prototyping Core at the Wyss Institute. The Ti molds were exposed to 3 mins of oxygen plasma to clean organic residue. The dextran solution (10% dextran in 25% isopropyl alcohol, both chemicals from SigmaAldrich, St. Louis, MO) was spin-coated on the Ti mold as a water-soluble sacrificial layer. Soft PDMS mixture was mixed in 1:10 ratio of Sylgard 184 and Sylgard 527 (both chemicals from Dow Corning, Midland, MI), and then was spin-coated on top of the dextran layer as the bottom layer of the tissue-engineered ray fin (fig. S3A). This tissue-engineered ray substrate was incubated at 65 ºC for 4 hours. Second, the 2:1 stiff PDMS mixture (Sylgard 184: 527 ratio) was filled in the cavity of the Ti mold, and the residue of the mixture was removed with a thin film spatula (fig. S3B). The tissue-engineered ray

substrate was again incubated at 65ºC for 4 hours. Third, the 9-nm Ti, 17-nm gold (Au), and 1-nm Ti layers were thermally evaporated on the tissue-engineered ray substrate through a shadow mask using an e-beam evaporator (Denton Vacuum, Moorestown, NJ) to form the gold skeleton of the engineered ray (fig. S3C). The shadow mask was designed to have the same directionality in terms of skeletal structure as the animal batoid, and was fabricated with a 100-μm stainless steel shim (McMaster-Carr, Elmhurst, IL). The skeleton pattern was engraved by a UV laser engraver (ProtoLaser U3, LPKF Laser & Electronics, Germany). The structures of gold skeleton and tissue-engineered ray body were aligned by matching the marks of the shadow mask and the Ti mold. Fourth, 1:5 soft PDMS mixture (Sylgard 184: 527 ratio) was spin-coated on the tissue-engineered ray substrate to form the top layer of the ray fin, which was then incubated at 65 ºC for 4 hours, and annealed at 190 ºC for 30 mins (fig. S3D). Fifth, the PDMS layers of the tissue-engineered ray substrate were laser cut with a CO_2 laser engraver (VersaLaser 2.0, Universal Laser Systems, Scottsdale, AZ) to form the ray outline (fig. S3E). Sixth, human fibronectin (FN) pattern (BD Biosciences, Sparks, MD) was microcontact printed on the ray substrate (fig. S3F). PDMS stamps for patterning FN were designed to have mesoscale serpentine patterns overlaid with microscale line patterns (fig. S4). The mesoscale serpentine patterns were designed to have > 100 μm gap to prevent cardiac cells from spanning over the parallel sections. The microscale line patterns were designed to have 15 to 25 μm wide lines and 2 to 4 μm gaps to generate anisotropic microstructure of cardiac tissue with the same directionality of the pectoral fin skeletal structure. PDMS stamp structure was fabricated with 5 μm thick SU-8 photoresist mold (Microchem, Newton, MA) using soft-lithography as previously described (*14*). The stamps were incubated with fibronectin (50 μg/ml in deionized water, BE Biosciences, Sparks, MD) for 1 hour and dried with air. The fibronectin pattern was transferred to the tissue-engineered ray substrate by precisely aligning and contacting the stamp to the body outline on the ray substrate under a stereomicroscope (MZ8, Leica, Germany). The isolated ventricular myocytes (fig. S3G) were seeded on the ray substrate at a density of 1 million cells per well of a 6-well dish (fig. S3H). After 1 day, the sample was washed twice with phosphate buffered saline (PBS) and reincubated in culture medium with 10% fetal bovine serum (FBS) and lentiviral vectors encoding for ChR2-eYFP (fig. S3I). On day 2 (post-transduction day 1), the sample was washed twice with PBS and incubated with culture medium with 2% FBS (fig. S3J). On day 4 (post-transduction day 3), the engineered ray was gently peeled off with a tweezer (fig. S3K). The floating engineered ray was then turned over (fig. S3L) in Tyrode's solution (1.192 HEPES, 0.040 NaH2PO4, 0.901 glucose, 0.265 CaCl2, 0.203 MgCl2, 0.403 KCl, 7.889 NaCl [g/l], pH 7.4, all chemicals from SigmaAldrich, St. Louis, MO) (fig. S3L).

Immunofluorescent staining of the muscle structure of the tissue-engineered ray

The tissue structure of the tissue-engineered ray was visualized with immunofluorescence. The harvested cardiomyocytes were cultured on PDMS-coated glass coverslips with FN patterns for 4 days and transduced with lentivirus containing ChR2-eYFP for 3 days. The samples were washed with PBS at 37ºC, fixed in PBS with 4% paraformaldehyde and 2.5% TritonX-100 for 12 mins at 37ºC and rinsed with PBS 3 times. Staining with mouse anti-sarcomeric α-actinin monoclonal primary antibody (Sigma-Aldrich, St. Louis, MO) was conducted for 1 hour at room temperature, and an

additional staining with secondary antibody against mouse IgG conjugated to Alexa-Fluor 546 (Invitrogen, Carlsbad, CA), DAPI (Invitrogen, Carlsbad, CA), and anti-GFP antibody conjugated to FITC (Abcam, UK) was conducted for 1 hour at room temperature. The samples were rinsed with PBS 3 times before and after primary and secondary staining. The samples were mounted on glass slides with ProLong Gold antifade mountant (Invitrogen, Carlsbad, CA).

Imaging and analysis of the structure of the batoid and the tissue-engineered ray

Histology sections and fluorescently labelled tissue-engineered rays were imaged with a VS120 Olympus Slide Scanner and an Olympus confocal microscope (Olympus, Center Valley, PA) with appropriate filter cubes. Images were taken with 10x, 20x, or 40x objective lenses. The angle distribution of sarcomeric α-actinin was analyzed using a MATLAB code based on fingerprint detection as previously reported (*34*).

Digital radiographs of batoid *P. orbignyi* and the tissue-engineered ray were taken with a digital x-ray machine at the Digital Imaging Facility of the Harvard Museum of Comparative Zoology and with a micro-computed tomography system (X-Tek MicroCT system, NiKon, Japan) at the Center for Nanoscale Systems at Harvard University, respectively. Planar x-ray images of the tissue-engineered ray were constituted using software (VGStudio MAX, Volume Graphics GmbH, Germany).

Fabrication parameter calibration for spin-coating PDMS mixtures

Sylgard 184 and Sylgard 527 elastomers (Dow Corning, Midland, MI) were mixed at 10:1 and 1:1 base to curing agent ratios, respectively. The PDMS mixtures were mixed in 1:10 and 1:5 ratios of Sylgard 184 and 527, spin-coated on glass coverslips with varying spin speed, and cured at 65 ºC oven for 4 hours. The film thickness was measured with a stylus profilometer (P-16+, KLA-Tencor, Milpitas, CA).

Elastic modulus measurement of PDMS mixtures

Modulus measurements on PDMS preparations were conducted on a biaxial mechanical tester (BioTester, CellScale Inc., Waterloo, ON). 5x5mm PDMS samples of approximately 2.5 mm thickness were subjected to 15% strain at 1%/s using 2.5mN load cells. Force and displacement measurements and corresponding images were recorded at 15 Hz. PDMS moduli were measured from the slope to the linear stress vs strain curve.

Optogenetics: plasmid constructs and viral transduction

A lentiviral vector containing EF1α-ChR2-eYFP was based on the FCK(1.3)GW plasmid. To drive cardiac-specific expression, the cardiac troponin T (cTnT) promoter was PCR amplified (-493 to +192, provided as a gift by Dr. Jim Lin, U. Iowa) and ligated into the vector via PacI and AgeI restriction enzyme sites. The plasmid was amplified and purified using the endotoxin-free plasmid preparation kit (Qiagen, Netherlands). The recombinant lentiviruses were produced by transfecting 293FT cells (Invitrogen, Carlsbad, CA) with cTnT-ChR2-eYFP, pMD2.G, and pCMVdeltaR8.74 in the Vector Core facility at University of North Carolina at Chapel Hill, as previously described (*35*). The viral titer after harvest was between 7×10^6 and 4×10^7 infectious units (IU) per ml.

Harvested cardiomyocytes and non-cardiomyocytes were cultured in an FN coated 6-well plate and in a T-75 culture flask for 24 hours, respectively. Both cardiomyocytes

and non-cardiomyocytes were infected in vitro with lentivirus (3-5 × 10^6 IU/ml), and incubated at 37ºC for 2 to 5 days before flow cytometry. Sham-treated cardiomycoytes were incubated with culture media. Flow cytometry was conducted using a BD LSRII analyzer in the Bauer Core Facility at Harvard University. Signals of side scatter, forward scatter, and eYFP were monitored to determine positive (ChR2-eYFP) and negative transfection for infected cardiomyocytes, infected non-cardiomyocytes, and naïve cardiomyocytes.

Electrophysiological recording of photosensitive activity in cardiac cells with patch-clamp

Photosensitive electrophysiological activities of ChR2 expressing cardiomyocytes were recorded with a planar patch-clamp system (Port-a-Patch, Nanion Technologies GmbH, Germany) and an amplifier (EPC-10 Double, HEKA Instruments Inc, Holliston, MA) using planar borosilicate glass chips with 2-3.5MOhm pipette resistance (NPC-1, Nanion Technologies GmbH, Germany). Solid-state light sources (Spectra X, Lumencor, Beaverton, OR) were implemented to generate optical pulses with six wavelength bands (390/18, 438/24, 470/22, 542/27, 593/40, and 632/22 nm, Semrock, Rochester, NY). The light sources were connected to the EPC-10 amplifier through digital input into a data board system (USB-6501, National Instruments, Austin, TX), so a delay time between the patch-clamp system and light sources was minimized to less than 1 ms. Light was delivered to the cardiomyocytes through the optical fiber (400 μm diameter, NA 0.48, Doric lens, Canada) that was located 500 μm above the patch-clamp chip using fine control of a 3-axis manipulator (Zaber, Canada). All experiments were performed at 37ºC.

The ChR2-expressing cells cultured on 6-well plates were isolated with 0.5% trypsin (Invitrogen, Carlsbad, CA) and resuspended in extracellular buffer solution (140 NaCl, 4 KCl, 1 MgCl2, 2 CaCl2, 5D-glucose monohydrate, 10 HEPES [mM], pH 7.4). As soon as extracellular buffer solution and intracellular buffer solution (50 KCl, 10 NaCl, 60 KF, 20 EGTA, 10 HEPES [mM], pH 7.2) were introduced into the chip, cell-suspended solution (0.5μL with 1M cells /ml) was flown into the chip. The pressure inside the chip was adjusted automatically to establish greater than 1 GOhm sealing resistance.

Photocurrents of the ChR2-expressing cells were measured in voltage-clamp at -70 mV, while 300-ms duration light pulses were applied on the cells with varying wavelength and intensities. Action potentials of the ChR2-expressing cells were recorded in the current clamp, while 10-ms duration light pulses were applied to the cells with varying pacing frequencies.

Optical mapping of muscle circuit

Calcium activities of the muscle circuit were monitored with a calcium indicator, X-Rhod-1 (Invitrogen, Carlsbad, CA), using a modified tandem-lens macroscope (fig S14A). The tandem-lens macroscope (Scimedia, Costa Mesa, CA) was equipped with a high speed camera (MiCAM Ultima, Scimedia, Costa Mesa, CA), a plan APO 0.63× objective, a collimator (Lumencor, Beaverton, OR) and a 200 mW mercury lamp for epifluorescence illumination (X-Cite exacte, Lumen Dynamics, Canada). To prevent overlay of the excitation light wavelength of calcium transients measurement with the excitation of light sensitive ion channels, we used a filter set with longer wavelengths

than the ChR2 excitation wavelength (excitation filter: 580/14 nm, dichroic mirror: 593 nm cut-off, emission filter: 641/75, Semrock, Rochester, NY).

The muscle circuit at post-transduction day 3 was incubated with 2 μM X-Rhod-1 for 30 min at 37 ºC, rinsed with culture medium with 2% FBS to remove nonspecifically associated dye, and incubated again for 30 mins to complete de-esterification of the dye. The muscle circuit was rinsed with Tyrode's solution and mounted on a heating stage (Warner Instruments, Hamden, CT) of the tandem-lens macroscope. The temperature of the solution was maintained at approximately 37 ºC. The calcium images were acquired at a frame rate of 200 Hz with a field of view of 16 by 16 mm. Optical stimulation was applied to the anterior part of the muscle circuit through the optical fiber (400 μm diameter, NA 0.48, Doric lens, Canada), located 500 μm above the patch-clamp chip, using fine control of a 3-axis manipulator (Zaber, Canada).

Post-processing of the raw calcium data was conducted with custom software written in MATLAB (MathWorks, Natick, MA). A spatial filter with 3 × 3 pixels was applied to improve the signal-noise ratio. Activation time and 30, 60, and 80% repolarization times were calculated at the average maximum upstroke slope, as well as the average recovery time at 30, 60, and 80% of multiple pulses over a 5 second recording window. The total activation time was determined as the difference between activation times at the last and the first activation sites along the single fin. Activation area was calculated as the area of the active tissue on the repolarizing phase, of which calcium signal was under 80% of peak amplitude, when the single calcium wave propagated through the muscle circuit.

Particle imaging velocimetry (PIV) of the tissue-engineered ray

Flow field generated by the tissue-engineered ray was monitored using PIV. In PIV, the fluid motion was determined by visualizing the movement of reflective and neutrally buoyant particles over a thin sheet of light illuminated by a laser (fig. S14B). We seeded silver coated particles with 5-15 μm diameter and neutral buoyancy (1.08 g/mm density, Cospheric LLC, Santa Barbara, CA) in Tyrode's solution in a water chamber. The temperature of Tyrode's solution in the water chamber was maintained by a hot plate (VWR International, Radnor, PA) at 37 ºC. The tissue-engineered ray was located in a water chamber with a minimum distance (> the body length of the ray) away from the walls as well as the air-liquid interface to minimize the boundary effect from the walls of the chamber and the air-liquid interface. 470-nm light pulses were applied to the anterior part of the tissue-engineered ray through the optical fiber (400 μm diameter, NA 0.48, Doric lens, Canada). While the particles were illuminated by the thin sheet of light made by the light from a 5mW 650-nm laser pointer (Staples, MA) through a concave cylindrical lens (Thorlabs, Newton, NJ), the motions of the particles were recorded at 100 frames per second with a sCMOS camera (Pco.edge, PCO AG, Germany) that was installed perpendicular to the illuminated sheet. Movie S10 is an example of PIV recording. Velocity field was calculated by performing correlation analysis on the positions of seeded beads between successive video frames using an open-source software (PIVlab, (*36*)) written in MATLAB (MathWorks, Natick, MA).

3D kinematics and flow visualization in free swimming in the Little skate

All experimental studies of Little Skates (*Leucoraja erinacea*) were conducted in accordance with the guidelines of Harvard University's Animal Care and Use Committee. Animals averaged 7.3 cm disc length and 23.7 grams. For analysis of swimming kinematics, individual Little Skates swam in a recirculating flow tank at speeds of 0.5 to 2.0 body lengths per second. Two synchronized Photron PCI-2014 high-speed video cameras recorded dorsal and lateral images of wing motion at 250 Hz, and videos were calibrated in three dimensions using the standard DLT protocol as in our previous research on fish swimming kinematics (*37-39*). Movie S1 provides an example of lateral view kinematic video data. Quantification of the motion of 8 points on the wing in three dimensions through time allowed reconstruction of the amplitude of wing motion in comparison to the synthetic batoid fish.

Particle image velocimetry of the body and wake of freely-swimming Little Skates was conducted as in our previous research on the fluid dynamics of freely- swimming fishes and robotic systems (*40-43*). To analyze the effect of wing and body motion on fluid flow patterns, individual Little skates swam in a recirculating flow tank at speeds of 0.5 to 2.0 body lengths per second. A Photron PCI-2014 high-speed video camera recorded lateral-view images at 1000 Hz. A 5W continuous wave Coherent argon-ion laser provided illumination of the water movement. We generated a vertical light sheet that illuminated the body and wing from below, although the thin and translucent character of the Skate wing allowed laser light to pass through and illuminate particles passing above the wing. Seeding with 50 um plastic spheres provided reflective elements that tracked fluid motion. Video images were imported into DaVis software (v. 8.2, LaVision Inc., Goettingen, Germany), where they were calibrated and processed via an FFT-based cross-correlation routine (two-pass, 16 x 16 pixel interrogation area with 50% overlap) that analyzed particle movement to produce a two-dimensional array of fluid velocity vectors. Movie S11 provides an example of the lateral view flow visualization data.

Optical stimulation for locomotion control of the tissue-engineered ray

To pace the tissue-engineered ray, two light emitting diode (LED) sources (465-nm, Doric Lenses Inc, Canada) were used. Light pulses for pacing individual fins were delivered through mono fiber optic cannulas (flat end, 400 μm diameter, NA 0.48, Doric Lenses Inc, Canada) mounted 5-7 mm apart, so as to minimize signal crosstalk, while ensuring direct shining over the anterior part of the ray. To generate synchronous and asynchronous pacing pulses for controlling the locomotion of the tissue-engineered ray, the LED sources were independently controlled by analog signals that were synthesized with an analog output module (NI 9264, National Instruments, Austin, TX) by a custom software written in LabVIEW (National Instruments, Austin, TX). In addition, the analog output module was triggered by digital trigger signals that were generated by two push button switches through a digital board (USB-6501, National Instruments, Austin, TX), shown in fig. S14C, allowing the digital signals to switch from synchronous to asynchronous pacing protocol or vice versa without time-delay.

Electrical field stimulation for locomotion control of tissue-engineered ray

A voltage pulse generator (MyoPacer Cell Stimulator, IonOptix, Milton, MA) was used to deliver the electrical field through two U-shaped platinum electrodes (Sigma-

Aldrich, St. Louis, MO) to induce the global contraction of the entire fin of the tissue-engineered ray. Two U-shaped platinum electrodes measuring 8 cm long generated monophasic square pulses at 1.5Hz, 2.5 V/cm and 10-ms duration for pacing the tissue-engineered ray.

Locomotion performance testing of the tissue-engineered ray

To test the locomotion performance of the tissue-engineered rays, they were placed in Tyrode's solution in 22 cm by 22 cm water chamber of which temperature was maintained at 35 ºC to 37 ºC by a hotplate (VWR International, Radnor, PA). The digital recordings of the swimming tissue-engineered rays were accomplished with a sCMOS camera (Pco.edge, PCO AG, Germany) coupled with a zoom camera lens (Thorlabs Inc, Newton, NJ) at 100 frames per second, and a digital single-lens reflex camera (D5200, Nikon, Japan) with a zoom camera lens (AF-S DX NIKKOR, Nikon, Japan) at 30 frames per second. The tissue-engineered ray was paced with optical point stimulation or electrical field stimulation at various pacing frequencies (1 to 3 Hz).

To conduct phototactic steering test of the tissue-engineered rays, they were placed in the water chamber, where multiple obstacles were placed with distance greater than the average turning radius of the tissue-engineered ray (4.5 cm). Locomotion of the tissue-engineered rays was controlled by frequency modulation of light pulses, which were switched independently from low to high frequencies or vice versa by two push-buttons operation. The temperature of Tyrode's solution was controlled at 35 to 37 ºC by a hotplate (VWR International, Radnor, PA). The digital videos were acquired with a digital single-lens reflex camera (D5200, Nikon, Japan) with a zoom camera lens (AF-S DX NIKKOR, Nikon, Japan) at 30 frames per second.

Video-tracking of the tissue-engineered ray

The digital videos recorded during locomotion experiments were converted to image stacks using a custom-made Matlab program (Mathworks, Natick, MA). The head and tail positions of the tissue-engineered rays were tracked by image processing software (ImageJ, NIH, Bethesda, MD). The linear and angular distances of the tissue-engineered ray were measured during each stroke generated by optical pulse, and the linear and angular speeds of the tissue-engineered ray were calculated by multiplying the measured distances by the given stimulation frequency.

The Student's t-test was applied to compare the swimming performance of various groups of tissue-engineered rays using a custom-made Matlab program (Mathworks, Natick, MA), and statistical software JMP (SAS, Cary, NC). In particular, an unpaired t-test was conducted for comparison of performance in tissue-engineered rays fabricated with various designs (fin thickness and body shape), while a paired t-test was used for comparison of performance in the same tissue-engineered ray stimulated with different methods (electrical field stimulation vs. optical point stimulation). Lower p-value than significance level, 0.05, was applied to conclude that the difference of the performance was statistically significant.

Durability measurement of the tissue-engineered ray

The tissue-engineered ray was released after 5 days in culture. We conducted measurements of locomotion speed in a 37ºC Tyrode's physiological salt solution for 15

minutes once a day. After each measurement the ray was transferred and incubated in a supplemented M199 cell media (Invitrogen, Carlsbad, CA) with 2% heat-activated fetal bovine serum (FBS) (Invitrogen, Carlsbad, CA) at 37ºC. The locomotion speed was measured with a digital single-lens reflex camera (D5200, Nikon, Japan) and zoom camera lens (AF-S DX NIKKOR, Nikon, Japan) at 60 frames per second, while synchronous optical point stimulation was applied to the anterior part of both fins at the light pulse frequency of 1.5 Hz.

Structural analysis of fin deflection amplitude of the tissue-engineered ray

The maximum amplitude of the fin deflection was calculated by modifying the previously reported method (*44*). First, we developed a method to obtain the *z*-projection length from *x*-projection length of the thin film by considering the geometric relation of the radius of curvature (r/L), the angle of the arc ($\theta = L/r$), the *x*-projection length (x/L), and the *z*-projection length (z/L) of the thin film subject to bending (fig. S15A). When the film lies flat on glass, the initial radius of curvature (r/L) and the angle of the arc ($\theta = L/r$) are infinite and 0, respectively. As the film is deflected, the radius of curvature decreases and the angle of the arc increases. As reported previously, the *x*-projection length (x/L) decreases as $x/L = r/L \sin(L/r)$ at $\theta < \pi/2$ and decreases as $x/L = r/L$ at $\theta > \pi/2$ (fig. S15B). But because the relation of the z-projection length and the angle of arc is $z/L = r/L\ (1-\cos(L/r))$ at $\theta < \pi$, the *z*-projection length increases until it reaches the maximum, 0.725, at $\theta = 2.331$, after which it decreases (fig S15B). At $\theta > \pi$, the *z*-projection length continuously decreases as $z/L = 2r/L$. From these geometric relations, we calculated the *z*-projection length directly from the x-projection length (fig. S15C) and the maximum *z*-projection length (z_{max}/L) to achieve while the thin film is deflected from straight line ($\theta = 0$),

$\frac{z_{\max}}{L} = \frac{r}{L}\left(1 - \cos\frac{L}{r}\right)$, if $\theta \leq 2.331$ or $x/L \leq 0.429$,

$\frac{z_{\max}}{L} = 0.725$, if $\theta > 2.331$ or $x/L > 0.429$.

We calculated the maximum fin deflection from the outline of minimum *x*-projection length, which was acquired by image-processing the overlaid frames from movie S6 (fig. S15D). We assumed that the tissue-engineered ray fin consisted of multiple thin films (j=1 to m) connected in parallel with length, L_j, and oriented in a radial direction of the outline of minimum *x*-projection length (purple in fig. S15E). In addition, we assumed that the deflection of the tissue-engineered ray body and fin, which are thicker than 27.6 μm (green in fig. S15E), is negligible, because the bending modulus of thin film is proportional to the cube of the thickness, and the fin region thicker than 27.6 μm has one order of magnitude higher bending modulus than the 12.8 μm thick fin region. We calculated the length, L_j, of each thin film as the distance between the fin outline (black) and the outline with 27.6 μm thickness (green in fig. S15E). We calculated the angle of the arc of jth thin film, Θ_j, as L_j/R_j, where R_j, radius of curvature of jth thin film, was calculated from the outline of the minimum *x*-projection length using the relation between the radius of curvature and the *x*-projection length of the thin film (fig. S15F). Then we calculated the maximum deflection at multiple points (i=1 to n) on the thin film (fig. S15G). The angle of the arc and the length of the thin film at ith point on jth thin film was calculated with $\theta_{i,j} = (i/n)\ \Theta_j$ and $l_{i,j} = (i/n)\ L_j$, respectively. By considering the relation of *x*-projection length and the maximum deflection, the maximum deflection at ith point on jth thin film was calculated with

$Z_{i,j} = R_j\left(1 - \cos\left(\frac{i}{n}\Theta_j\right)\right)$, if $\theta_{i,j} \leq 2.331$,

$Z_{i,j} = 0.725\frac{i}{n}L_j$, if $\theta_{i,j} > 2.331$.

Using this structural analysis, we calculated the maximum deflection pattern of the tissue-engineered ray (Fig. 3I) from the outline of the minimum *x*-projection length (fig. S15D).

Supplementary Text

Calcium activities in muscle circuits

Calcium traces extracted from calcium imaging confirmed that (i) calcium waves initiated by optical stimulation at the anterior part, propagated through patterned circuit from the anterior to posterior fins (fig. S6, A and B), (ii) the muscle circuit can be operated by light pulses with a wide dynamic range of pacing frequency (fig. S6C), and (iii) each muscle circuit of fins can be independently controllable (fig. S6D).

The muscle circuit was optimized such that the number of traveling waves present in the muscle circuits of the synthetic ray were similar to the operating range of batoids (*Taeniura lymma*: 0.87 to 1.93 (*20*) and *Potamotrygon orbignyi* : 1.10 to 1.65 (*22*)) (Fig. 2E). The number of waves can be tuned by controlling the pacing frequency or serpentine pattern density (number of parallel section serpentine patterns per given fin area) of a serpentine muscle circuit (Fig. 2E). As pacing frequency increases, the number of waves, calculated by multiplying the pacing frequency with the total activation time, increases parabolically rather than linearly (Fig. 2E), because calcium wave propagation speed decreases and total activation time increases (fig. S7E) due to shortening of the repolarization time at high pacing frequency. We compared muscle circuits without serpentine pattern (fig. S7A and movie S4), with intermediate (fig. S7B and movie S3) and dense serpentine patterns (fig. S7C and movie S4), and determined that both the total activation time (fig. S7E) and the number of traveling waves (Fig. 2E) increase with increasing density of the serpentine pattern, because of the increasing length of the circuit pathway. Additionally, serpentine pattern density decreases the number of cells (activation area) associated with wave propagation (fig. S7D) and reproducibility (standard error) of the number of traveling waves (Fig. 2E), which decreases the possibility of synchronization between two muscle circuits in fins. Thus, there is a tradeoff between contraction time reproducibility (low standard error) and overlap with batoids' operating range to optimize the muscle circuit design (Fig. 2E).

In order to evaluate the reliability of muscle circuits in activating the tissue to produce sustainable muscle contraction, we measured calcium transient durations (CaTD30, CaTD60, and CaTD80) as the time from the upstroke to 30, 60, and 80% of recovery, respectively (fig. S8, A to C), and amplitude of calcium signals in the various muscle circuit designs (fig. S8D). The durations were uniformly distributed over the muscle circuit (fig. S8B), and CaTD80 values and amplitudes were statistically independent with serpentine pattern shape (fig. S8, C and D), which demonstrates that the serpentine pattern does not affect the homogeneity of calcium handling.

Control of locomotion speed and direction by frequency modulation

To control undulatory locomotion of the tissue-engineered ray, we implemented a frequency modulation strategy. Upon synchronous optical stimulation, the previously

spontaneous uncoordinated motions became coordinated within 5 strokes (fig. S11A and movie S12). As soon as the stimulation was terminated, the tissue-engineered rays reverted to spontaneous uncoordinated fin motions (fig. S11B and movie S12). Synchronous pacing on both fins resulted in straight, forward travel (movie S13). The tissue-engineered ray maintained a stable cruising speed over a distance of 99.5 mm (more than 6 times the body length) with more than 80 strokes (fig. S12, A and D). The swimming speed of the tissue-engineered ray can be controlled by modulation of pacing frequency: 1.5-2Hz pacing maximized the speed, while 1 or 3Hz minimized the speed (fig. S12E and movie S14 to S16).

Asynchronous pacing resulted in directional turns (fig. S12, B, C, and F). For an effective directional turn, we paired pacing frequencies in right and left fins respectively, to maximize the difference of individual fin speed. Paired pacing frequencies of 1 and1.5Hz (movie S17) and 3 and1.5Hz (movie S18) were used because these produced minimum and maximum straight line swimming speed with the synchronous pacing. The tissue-engineered ray, stimulated by asynchronous pacing, was able to change direction, both clockwise (CW) and counter-clockwise (CCW), by generating an asymmetric undulating motion between left and right fins, as utilized by batoid fishes. For both CCW and CW turns, the tissue-engineered ray changed body direction up to 90 degrees (fig. S12F). When applying asynchronous pacing, it increased angular speed until reaching the stable speed (fig. S12F). In addition, both angular speed and turning radius are statistically independent of turning direction (fig. S12G).

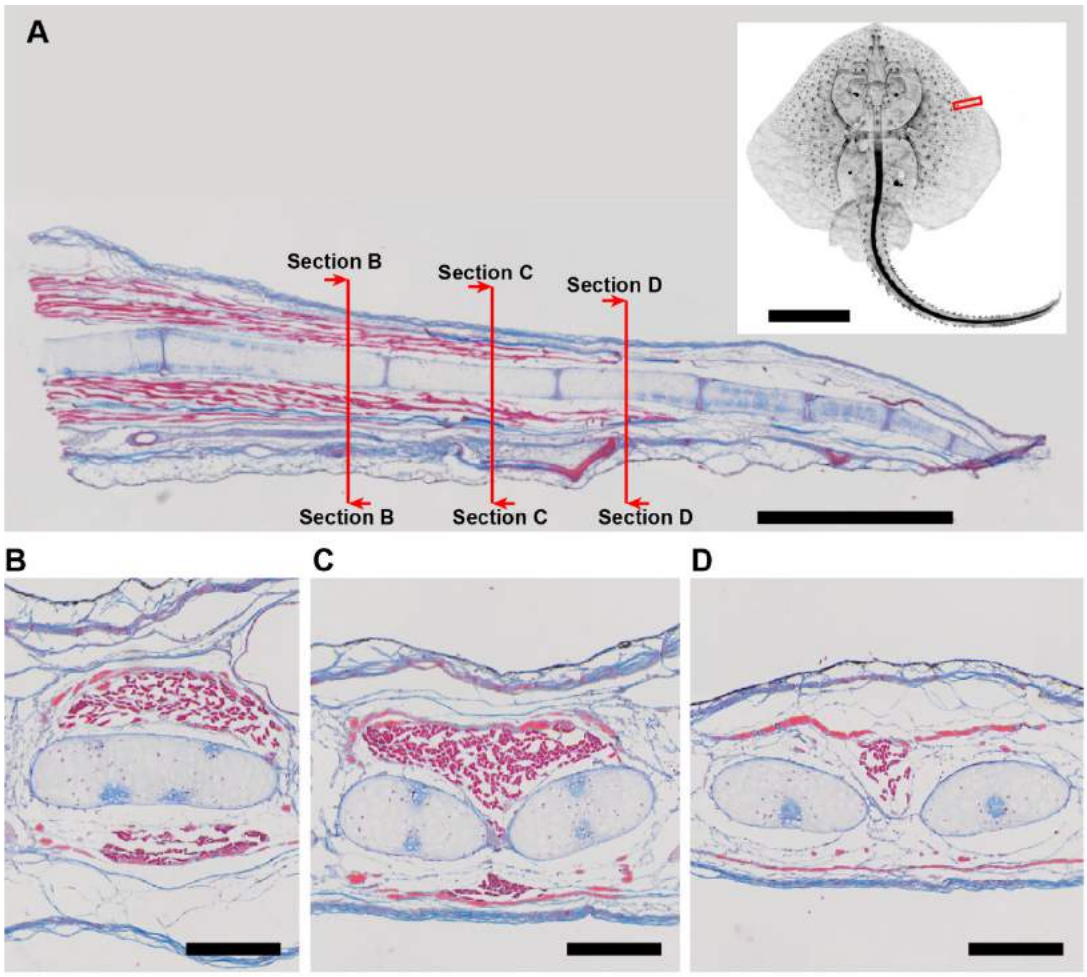

Fig. S1. Musculoskeletal structure of batoid fish, *Leucoraja erinacea*. (**A**) Histological coronal cross section of the skate's fin, indicated by red rectangle on inset. The inset is the radiography of a *L. erinacea.* Scale bars, 1 mm and 2 cm (inset). (**B to D**) Sagittal cross-sections at section B, C, and D along the long axis of a fin ray. Scale bars, 200 μm. Sections were stained with Mallory's trichrome: red and blue indicates muscle tissue and collagen, respectively. The pectoral fins increase flexibility along proximal-distal, by decreasing thickness of fin and rays and by branching and segmenting rays closer to the distal end.

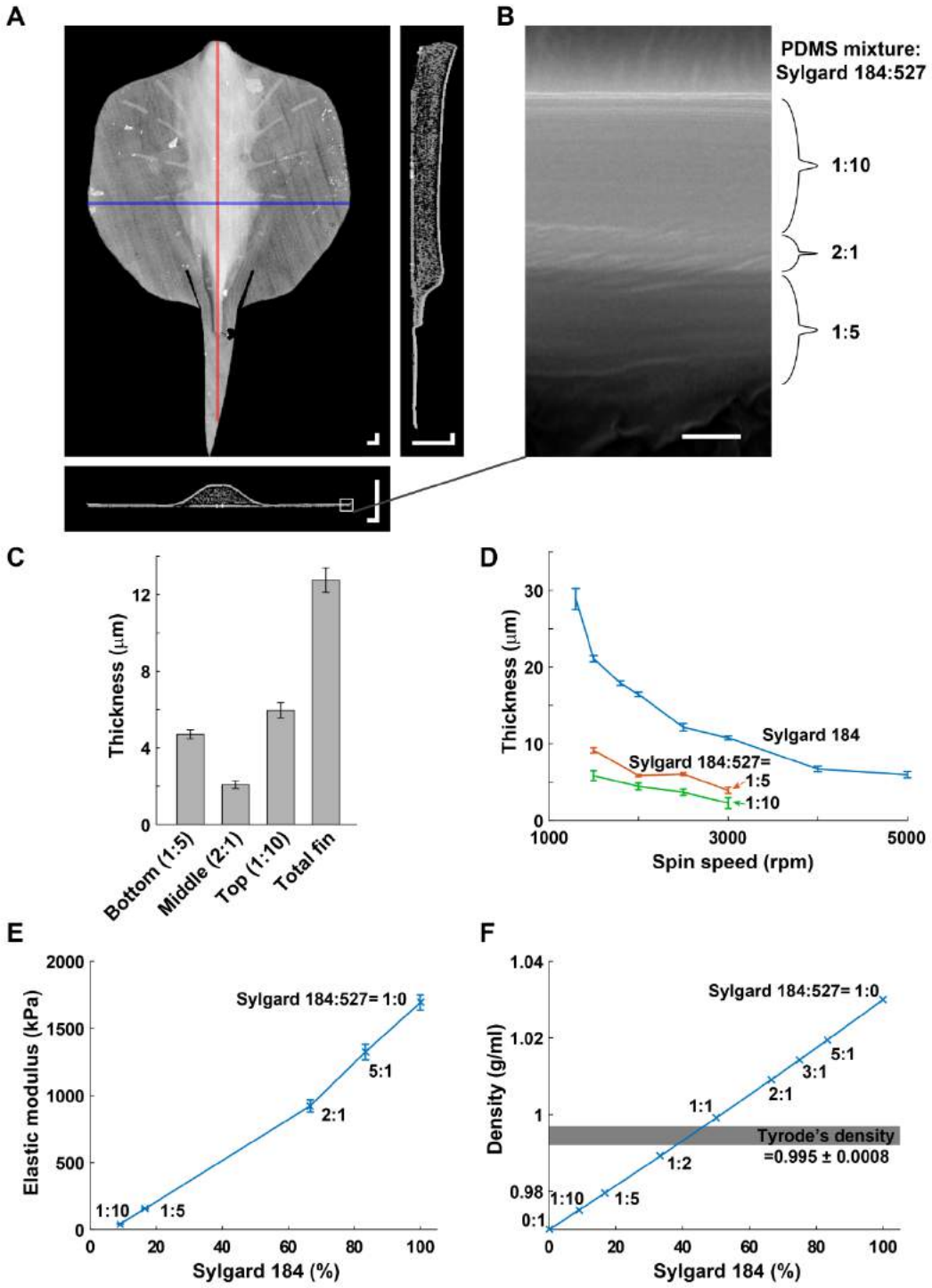

Fig. S2. Fabrication process optimization of elastomer body of the tissue-engineered ray. (**A**) The micro-computed tomography (micro-CT) scan images of the three dimensional structure of the tissue-engineered ray, which were reconstructed along horizontal (Middle), sagittal (Right) and coronal (Top) planes. The tissue-engineered ray has a three-dimensional structure of the dorsoventral disk, decreasing in thicknesses from proximal to distal and from anterior to posterior. Red and blue lines indicate the locations

of displayed sagittal and coronal planes, respectively, among the horizontal plane. Scale bars, 0.5 mm. (**B**) Scanning electron microscopy images of a sagittal cross-section of the tissue-engineered ray fin fabricated with three PDMS mixtures. Scale bar, 2 μm. (**C**) Thickness of three PDMS mixture layers in the final fin design of the tissue-engineered ray (n=11 fin patches with 3 tissue-engineered rays). (**D**) Spin coating speed calibration for thin film thickness of PDMS mixtures with various Sylgard 184 and Sylgard 527 ratios (n = 3 films). Desired PDMS thickness can be tuned by controlling the spin speed for desired deflection of fin rays. (**E**) Elastic modulus of PDMS mixture with various Sylgard 184 and Sylgard 527 ratios (n = 3 films). Elastic modulus can be tuned by controlling the mixture ratio for desired deflection of fin rays. (**F**) The comparison of densities of Tyrode's solution and the PDMS mixtures with various Sylgard 184 and Sylgard 527 ratios. To make the tissue-engineered ray with neutral buoyancy, we used dense PDMS mixtures (Sylgard 184:527 = 2:1) for the body to compensate for the light density of the ray fin made with light PDMS mixtures (1:5 and 1: 10). The density band of Tyrode's solution indicates upper and lower limits of measurement at 37ºC. (n = 5 Tyrode's solution). (**E** and **F**) The final composition of PDMS mixtures for body and fins was determined by trial and error: we created several batches of tissue-engineered rays with various compositions of PDMS mixture and tested their neutral buoyancy and swimming speed. All error bars indicate standard error of the mean.

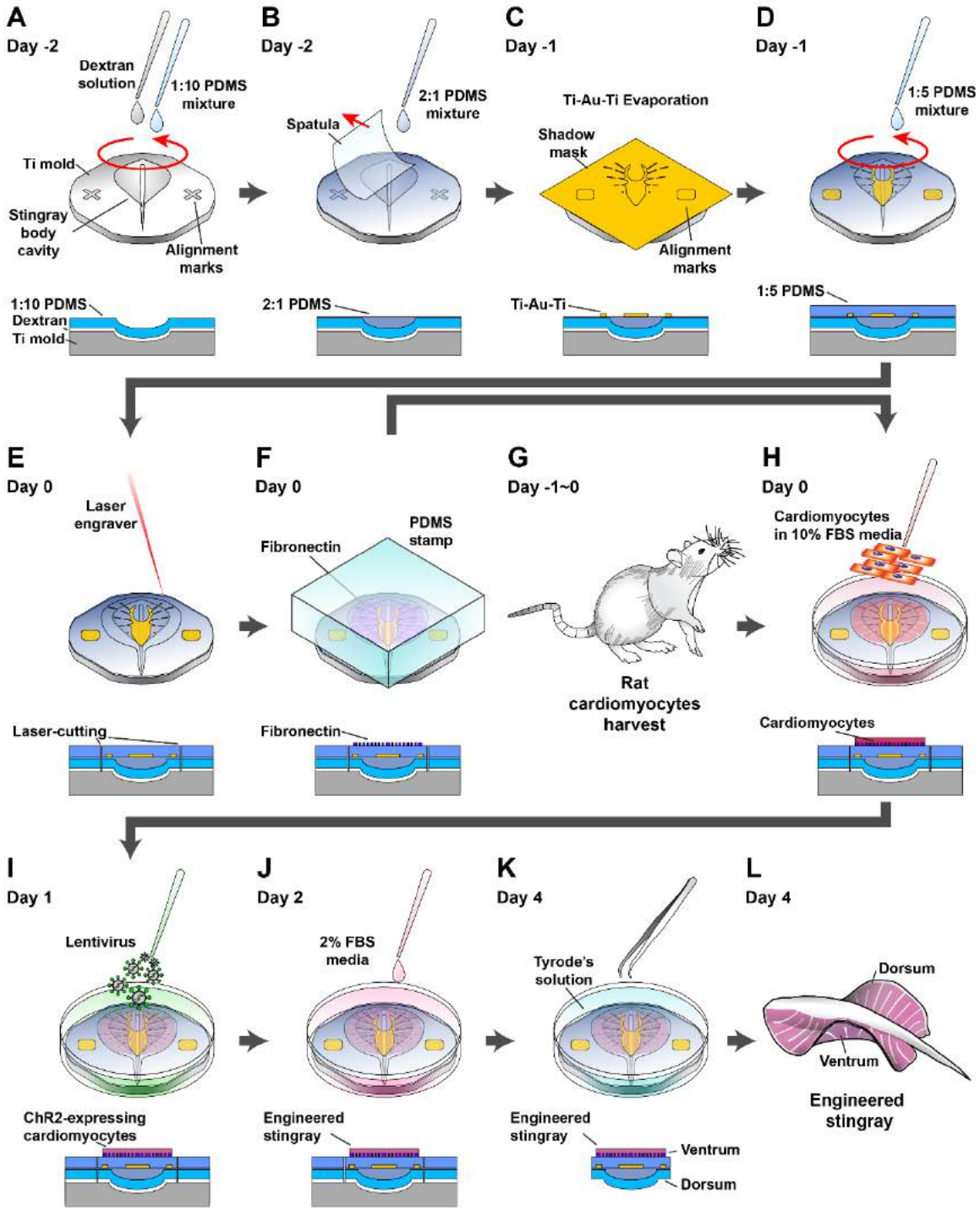

Fig. S3. Seven day fabrication process for the tissue-engineered ray. (**A**) The dextran solution (10% dextran in 25% isopropyl alcohol) and 1:10 soft PDMS mixture (Sylgard 184: 527 ratio) were sequentially spin-coated on a titanium (Ti) mold as a water-soluble sacrificial layer and bottom layer of the ray fin, respectively. This tissue-engineered ray substrate was incubated at 65ºC for 4 hours. (**B**) The 2:1 stiff PDMS mixture was filled in the cavity of the Ti mold that defined the body shape of the tissue-engineered ray, and the residue of the mixture was removed with a thin film spatula. The tissue-engineered ray

substrate was incubated at 65ºC for 4 hours again. (**C**) Ti, gold (Au) and Ti layers were thermally evaporated on the tissue-engineered ray substrate through a shadow mask to form the gold ray. (**D**) 1:5 soft PDMS mixture was spin-coated on the tissue-engineered ray substrate to form the top layer of the ray fin, incubated at 65 ºC for 4 hours, and annealed at 190 ºC for 30 mins. (**E**) The PDMS layers of the tissue-engineered ray substrate were laser cut to form the outline of the tissue-engineered ray. (**F**) Human fibronectin was patterned by microcontact printing. (**G**) Cardiac cells were isolated from ventricles of two day old neonatal Sprague-Dawley rats. (**H**) The tissue-engineered ray substrate was seeded in 6-well plates with 1 million cells. (**I**) After 1 day, the sample was washed twice with phosphate buffered saline (PBS) and reincubated in culture medium with 10% fetal bovine serum (FBS) and lentiviral vectors encoding for ChR2-eYFP. (**J**) On day 2 (post-transduction day 1), the sample was washed twice with PBS and incubated with culture medium with 2% FBS. (**K**) On day 4 (post-transduction day 3), the tissue-engineered ray was gently peeled off with tweezers. (**L**) The floating tissue-engineered ray was then turned over in Tyrode's solution.

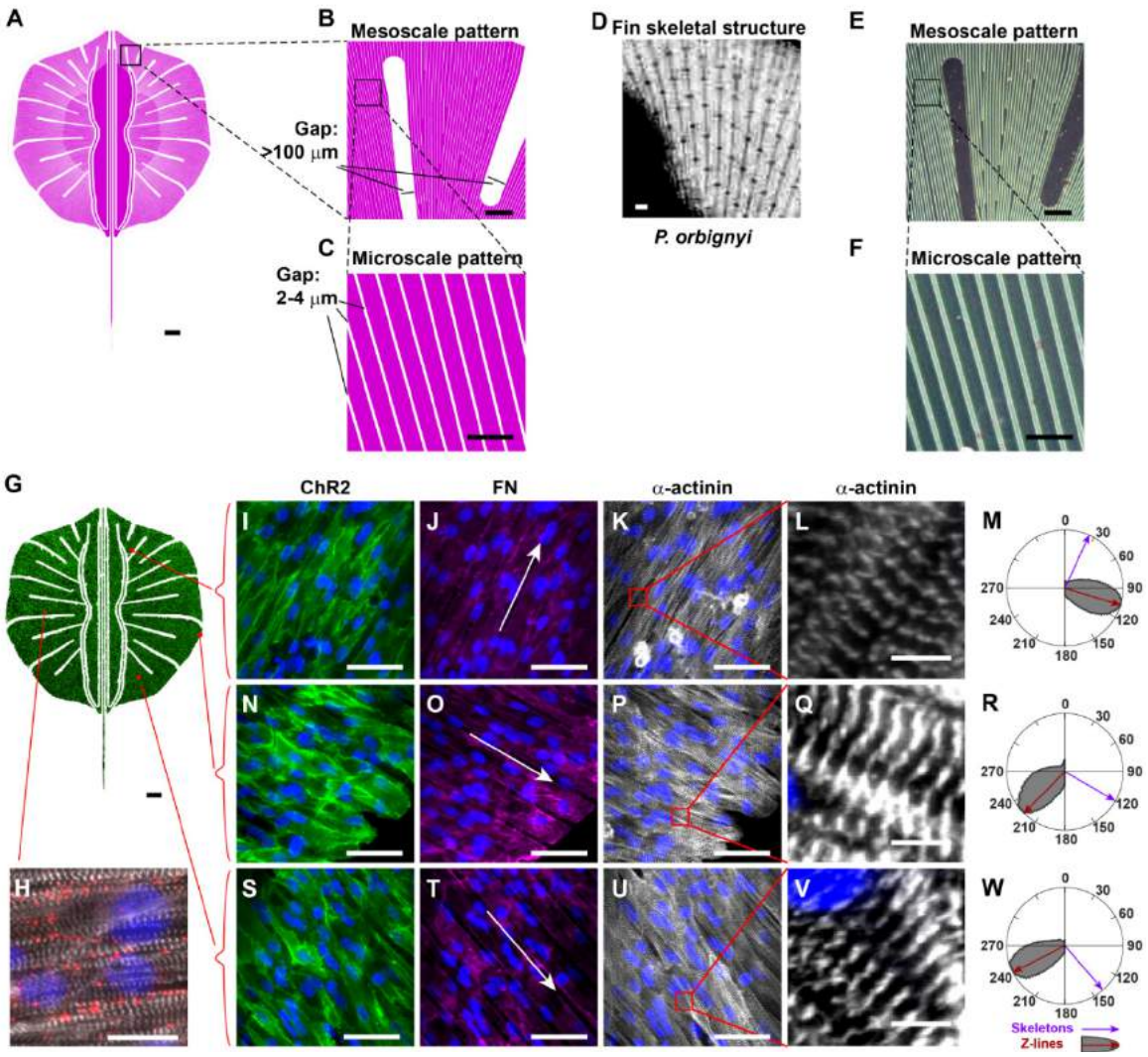

Fig. S4. Muscular structure design of the tissue-engineered ray. (**A to C**) Micro-contact printing mask design for patterning fibronectin (FN). Mask design consists of mesoscale serpentine patterns (**B**) overlaid with microscale line patterns (**C**). The mesoscale serpentine patterns are designed to have a gap wider than 100 μm between parallel sections, while the microscale line patterns are designed to have 15 to 25 μm wide lines with a 2 to 4 μm gap. In the mesoscale serpentine patterns, a gap wider than 100 μm is required to prevent cardiac cells from spanning over the parallel sections. The mesoscale serpentine patterns guide propagation of the action potential wave front through the tissue, and the microscale line patterns are used to generate laminar, anisotropic tissue. (**D**) The pectoral fin skeletal structure of *P. orbignyi*, having radially emanating rays. The image is a radiography of the anterior part of the fin in the horizontal plane. In order to align cardiac tissue with the skeleton rays of the tissue-engineered ray, we designed the microscale line patterns of FN aligned with the pectoral fin skeletal structure of *P. orbignyi*. (**E** and **F**) Optical microscope images of a PDMS stamp containing mesoscale serpentine patterns (**E**) and microscale line patterns (**F**). (**G** to **W**) Immunofluorescence images show that the muscular structure of the tissue-engineered ray ge

nerated by micro-contact printing matched the FN mask pattern (**A**). (**G**) The mesoscale pattern of FN induced clear serpentine tissue formation, and the microscale line pattern of FN generated radially oriented anisotropic tissue. Close-up images of three areas in (**G**) with immunofluorescence of Connexin 43 (red in **H**), ChR2 (green in **I**, **N**, and **S**), FN (magenta in **J**, **O**, and **T**), and sarcomeric α-actinin (white in **K**, **P**, and **U**). Blue indicates nuclei. (**H**) The engineered muscle cells are electrophysiologically linked with gap junctions (Connexin 43). (**I**, **N**, and **S**) ChR2 is expressed prominently and uniformly over the tissue. The microscale line patterns (**J**, **O**, and **T**) of FN guide orientation of cardiac cells in the tissue (**K**, **P**, and **U**). The white arrows (**J**, **O**, and **T**) indicate the local orientation of the FN patterns. (**L**, **Q**, and **V**) Close-up images of **K**, **P**, and **U**, respectively. The sarcomere structures (Z-lines – red arrows – and associated distributions - gray regions) were aligned perpendicularly to the skeleton rays (purple arrows, **M**, **R**, and **W**). Scale bars, 1 mm (**A**, **D** and **G**), 200 μm (**B** and **E**), 50 μm (**C**, **F**, **I**, **J**, **K**, **N**, **O**, **P**, **S**, **T**, and **U**), 20 μm (**H**), and 5 μm (**L**, **Q**, and **V**).

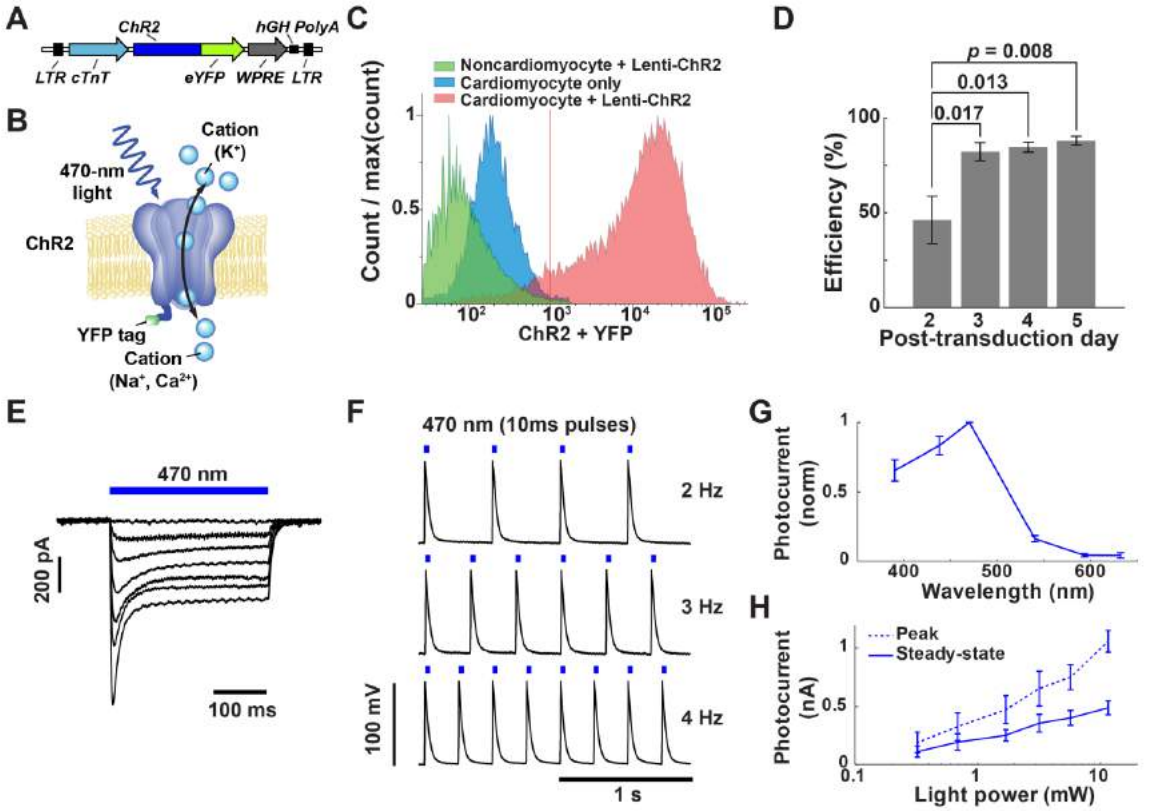

Fig. S5. Optogenetic cardiac tissue engineering. (**A**) Construct design of lentiviral vector for cardiac-specific transduction of channelrhodopsin-2 (ChR2). The lentiviral vectors for ChR2 transduction were constructed with a cardiac-specific promotor, cTnT promoter, and a fluorescence tag, eYFP. ChR2 is a light sensitive cation channel, opening the channel upon blue light and allowing the flow of cations (**B**). (**C**) Cardiomyocyte-specific gene expression with cTnT promoter. The transduction efficiency of lentiviral vector containing ChR2 and cTnT promoter in neonatal rat ventricular myocytes (red, 88%, n=6) is significantly greater than in non-cardiomyocytes (green, 7.0%, n=2) or in sham-transduced neonatal rat ventricular myocytes (blue, 6.8%, n=5) on day 4 or 5 after virus injection. (**D**) Transduction efficiency at different post-transduction days (n=6 tissues with 3 harvests). Analysis for ChR2-eYFP expression shows that expression of ChR2 in cardiac cells significantly increased at post-transduction day 3 (Student's t-test $p<0.017$). (**E**) Photosensitive inward currents at a holding potential of -70 mV with 300 ms blue light (0, 0.3, 0.7, 1.7, 3.2, 5.7, and 12 mW intensities, from top to bottom). In particular, a 470 nm light elicited a strong ChR2-mediated inward current (1060 ± 94 pA). (**F**) ChR2 activation with 10-ms 470 nm light pulses of different frequencies elicits action potentials. We gained optical control of the membrane potential at a single cell level. (**G** and **H**) The dependence of the photocurrent on light wavelength and power. (**G**) Action spectra of ChR2 measured by patch-clamp. (n=5 cells with 3 harvests) (**H**) Photocurrents of ChR2 across light intensities. (n=5 cells with 3 harvests). Lentiviral transduction period (post-transduction day 3, **D**), light wavelength (470 nm, **G**), and light power (11.6 mW, **H**) were optimized. Error bars indicate standard error of the mean.

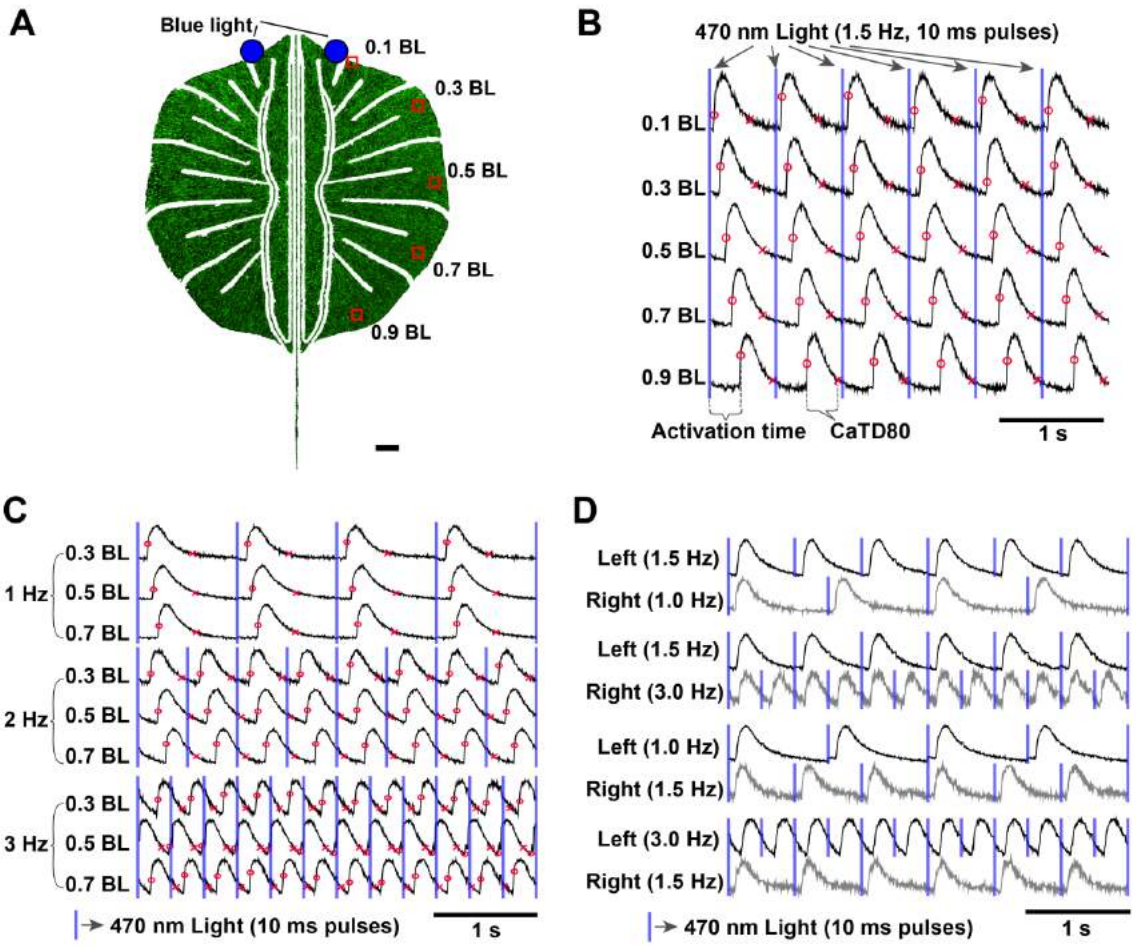

Fig. S6. Traces of calcium transients in muscle circuit of choice. (**A**) Muscle circuit with serpentine pattern of choice, scale bar, 1 mm. ChR2-eYFP (color: green) is expressed prominently and uniformly. Blue circles indicate optical stimulation sites. (**B**) Traces of calcium transients at different locations highlighted with red squares in (**A**) along anterior-posterior axis (0.1, 0.3, 0.5, 0.7, and 0.9 of body length from the front end of fins). Calcium waves initiated by local optical stimulation at the anterior part, propagated through serpentine pattern along anterior-posterior axis. Because action potentials trigger calcium-induced calcium release for excitation-contraction coupling, the propagation of calcium demonstrates sequential muscle activation in the muscle circuit. (**C**) Traces of calcium transients elicited with different pacing frequencies. Muscle circuit operates at a wide pacing range (1 to 3 Hz), which is similar with the wave frequency of batoids (*T. lymma*: 1.7 to 3 Hz (*20*) and *P. orbignyi* : 2.5 to 3.8 Hz (*22*)). (**D**) Independent activation of two muscle circuits by asynchronous pacing.

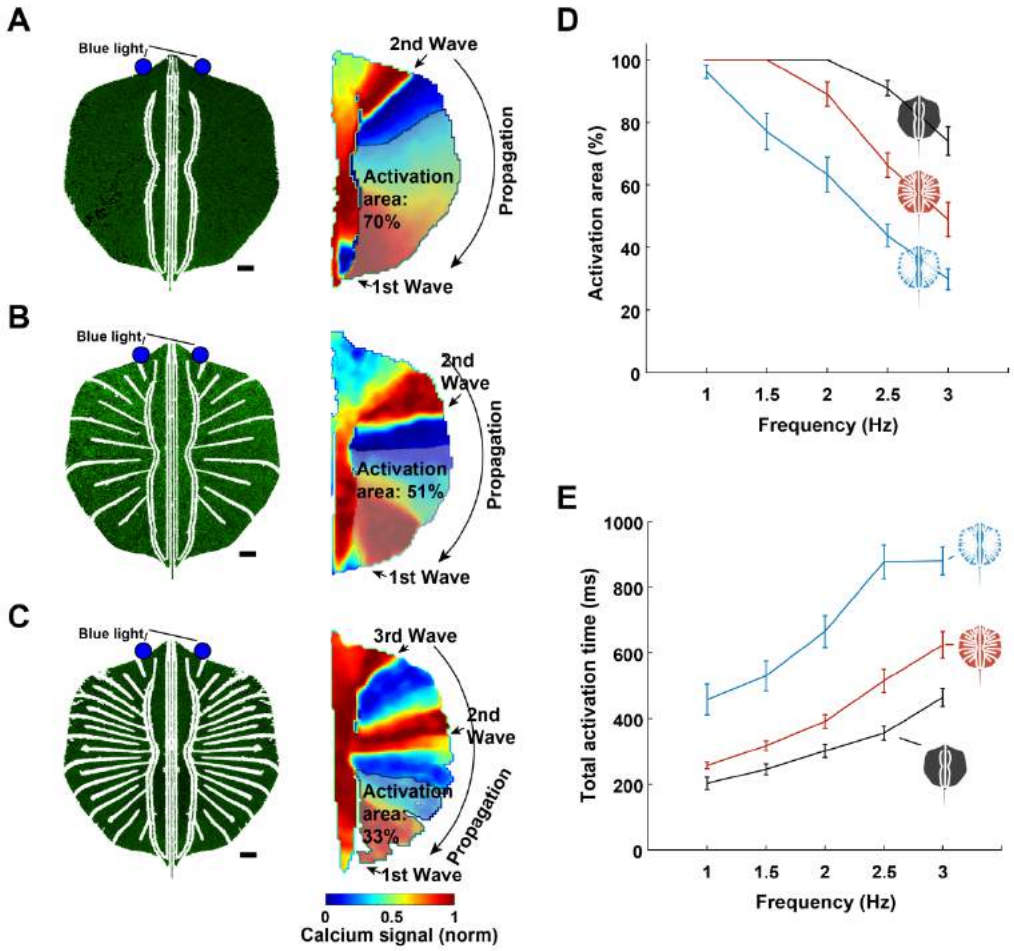

Fig. S7. Activation area and total activation time of muscle circuits. (**A** to **C**) Immunofluorescence and calcium imaging of muscle circuits expressing ChR2-eYFP (green) without serpentine pattern (**A**) and with intermediate (design of choice, serpentine pattern density: 10 parallel sections of serpentine patterns per fin, **B**) and dense serpentine pattern (serpentine pattern density: 20, **C**). The calcium imaging of the muscle circuit when the 1st calcium wave reaches the posterior part of the fin with 3 Hz optical pacing. The activation area is defined as the area of active tissue on the repolarizing phase, of which the calcium signal was under 80% of peak amplitude, when the single calcium wave propagated through muscle circuit. Dense serpentine patterns enhanced activation localization: a muscle circuit without serpentine pattern exhibits a 70% activation area, while the use of a serpentine circuit decreases the activation area (therefore improving localization) to 51% and 33%, depending on the serpentine density. (**D**) Activation area decreases with both pacing frequency and serpentine pattern density. Muscle circuits with serpentine patterns localize tissue activation, but produce weak contraction and increase the variation of the number of traveling waves (Fig. 2E), because the number of cells associated with muscle contraction and calcium propagation are reduced. (**E**) Total activation time as a function of the pacing frequency of muscle circuits with three different designs. The total activation time was determined as the difference between activation times at the last and the first activation sites along the single fin. Total activation time increases with pacing frequency. Lengthening propagation pathway of

action potential by adding more parallel sections in the muscle circuit increases total activation time. Black, red and blue indicate muscle circuits without serpentine, with intermediate and dense serpentines, respectively. Scale bars, 1 mm. Error bars indicate standard error of the mean (n=7 circuits).

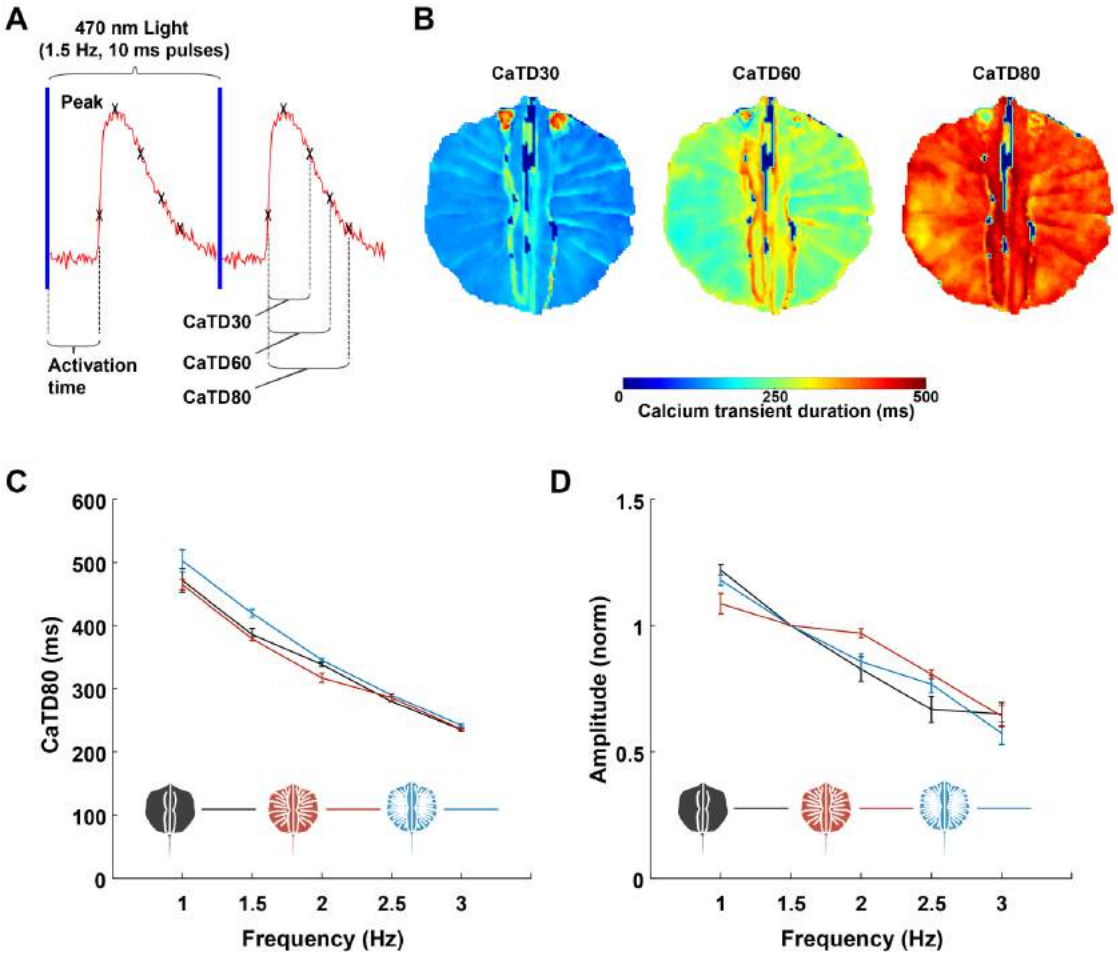

Fig. S8. Duration and amplitude of calcium transient in muscle circuits. (**A**) Calcium transient durations at 30, 60, and 80% repolarization (CaTD30, CaTD60, and CaTD80) were measured as the time from the upstroke to 30, 60, and 80% of recovery, respectively. (**B**) Spatial dispersion of CaTD30, CaTD60, and CaTD80 over the muscle circuit of choice. The durations were uniformly distributed over the muscle circuit with intermediate serpentine pattern. (**C**) CaTD80 decreases with pacing frequency, but it is statistically independent from muscle circuit design (analysis of covariance, ANCOVA, $p>0.05$). (**D**) The amplitude of calcium signals decrease with pacing frequency, but are statistically independent from muscle circuit design (ANCOVA, $p>0.05$). The duration and amplitude of muscle circuits demonstrate that the serpentine pattern does not affect the homogeneity of calcium handling. The amplitudes in each muscle circuit were normalized by the amplitude of calcium signal stimulated at 1.5 Hz. Calcium signal analysis was conducted from movie S3 and S4. Error bars indicate standard error of the mean (n=7 circuits).

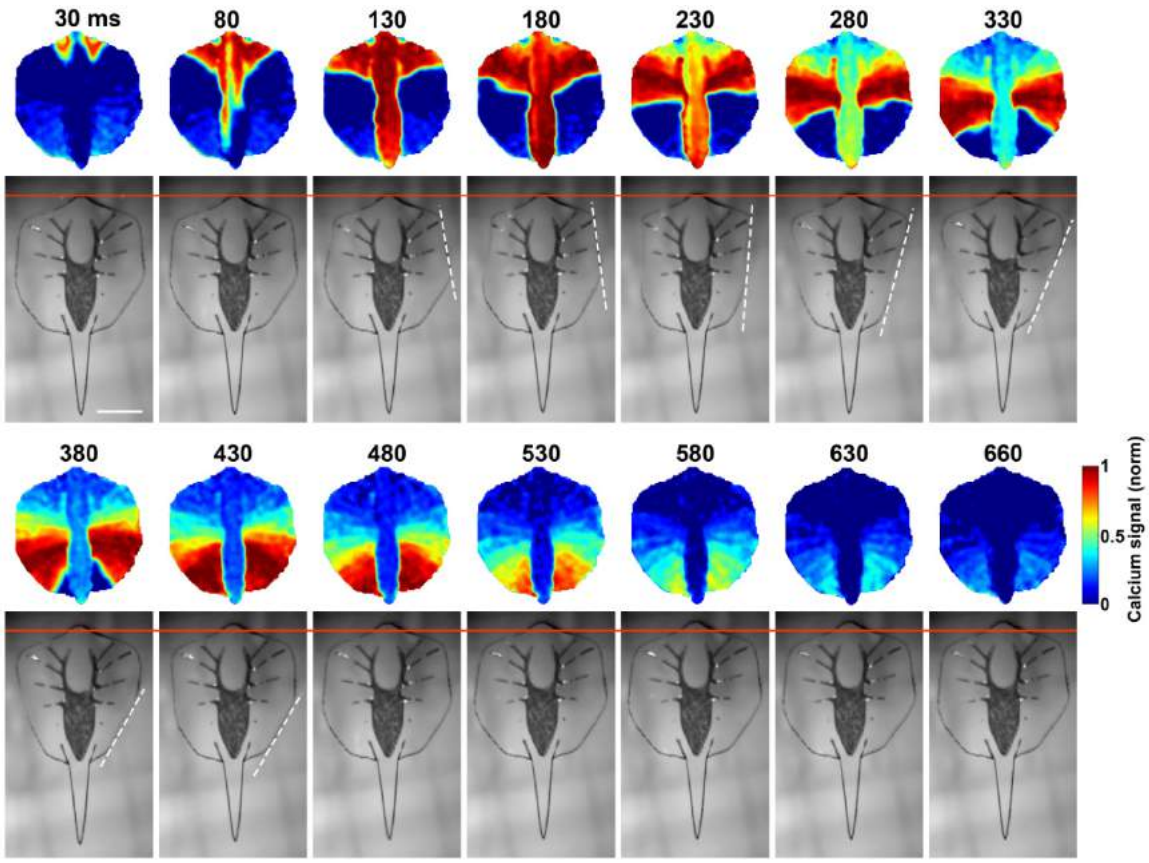

Fig. S9. Correlation between calcium activity (top) and undulating fin motion (bottom). Frames from movie S3 and S6 at various times during single stroke generated with 1.5 Hz optical stimulation. (Top) The calcium wave initiated by local optical stimulation at the anterior part, propagated through the pectoral fins. (Bottom) The tissue-engineered ray produced an undulatory wave that traveled along the fin in accordance with the calcium propagation, by changing the principal bending axis angle of the pectoral fin (dashed line). The undulatory locomotion speed of the tissue-engineered ray was minimal when the calcium wave was propagating, but the locomotion speed was increased after the calcium wave arrived at the posterior part of the fins. Its swimming speed was 1.72 mm/s. The time indicated in the figure corresponds to the time passed after a light pulse. The red line indicates the initial location of the tissue-engineered ray. Scale bars, 5 mm.

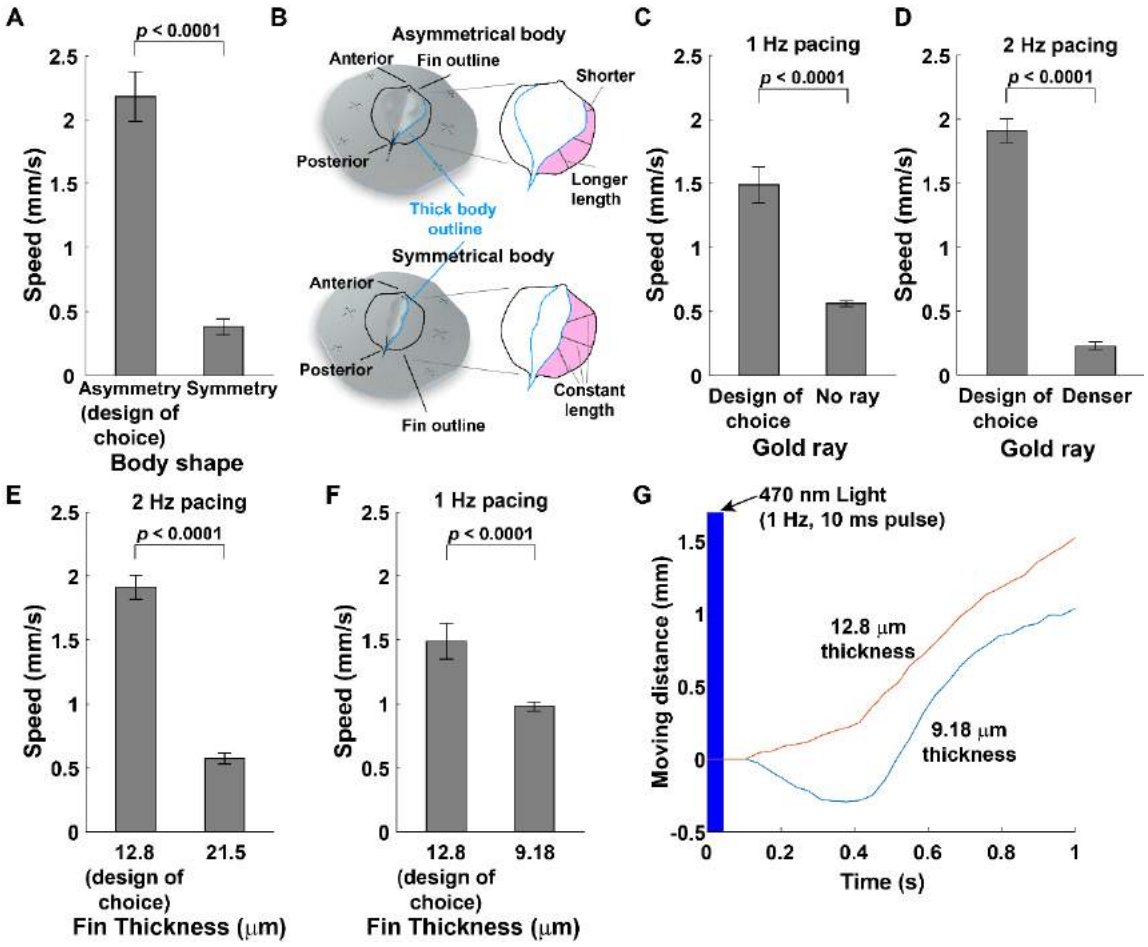

Fig. S10. The effect of fin structure on swimming performance. (**A** and **B**) Effect of body shape on swimming speed. (**A**) The tissue-engineered ray with the asymmetrical body improved swimming speed significantly, compared to one with a symmetrical body (Student's t-test, $p<0.0001$, asymmetry: n=237 strokes, and symmetry: n=19 strokes). The speed is calculated by video tracking the tissue-engineered ray's locomotion in movie S8. (**B**) Titanium mold designs to define an asymmetrical body (top) and a symmetrical body (bottom): The tissue-engineered ray characterized by an asymmetrical body (wider anterior and narrower posterior body) presents shorter anterior fins (denoted in pink) and wider posterior ones. The tissue-engineered ray with a symmetrical body (similar anterior and posterior widths) features fins with similar width along anterior-posterior axis. The tissue-engineered ray with the asymmetrical body has a dorsoventral disk with greater flexibility from anterior to posterior, while one with the symmetrical body has a disk with similar flexibility in the both anterior and posterior parts. The tissue-engineered ray with the asymmetrical body produced the asymmetric deflection pattern to minimize the drag at the front fin by increasing gradually the amplitude of contraction along the anterior-posterior axis, as the batoid fishes do (Fig. 3, H and I). (**C** and **D**) Effect of gold skeleton on swimming speed. The speed is calculated by video tracking the tissue-engineered ray's locomotion in movie S9. The tissue-engineered rays without a gold ray (**C**) and with a denser gold ray (**D**) decreased swimming speed significantly (Student's t-test, $p<0.0001$, design of choice: n=119, and no gold ray: n=20 strokes at 1

Hz pacing, and Student's t-test, $p<0.0001$, design of choice: n=137, and denser ray: n=7 strokes at 2 Hz pacing). The stresses generated by the cardiac muscle were insufficient for deflecting the fins embedding a skeleton characterized dense ray patterns, due to the increased stiffness of the substrate. (**E** to **G**) Effect of fin thickness on swimming speed. The speed is calculated by video tracking the tissue-engineered ray's locomotion in movie S9. (**E**) The tissue-engineered ray with thicker fins (21.5 μm) decreased swimming speed significantly (Student's t-test, $p<0.0001$, design of choice: n=137, and thick fin: n=39 strokes), because its cardiac muscle could not generate enough deflection due to increased stiffness of the substrate. (**F**) The tissue-engineered ray with thin fins (9.18 μm) reduced swimming speed significantly (Student's t-test, $p<0.0001$, design of choice: n=119, and thin fin: n=26 strokes). Due to the decreased stiffness of the substrate, the fin deflected with large amplitude. When the deflection amplitude exceeds a critical value, the benefit of the displacing larger masses of fluid is counterbalanced and dominated by the increased drag associated with a larger effective frontal area, thus impairing forward speed (**G**). Error bars indicate standard error of the mean.

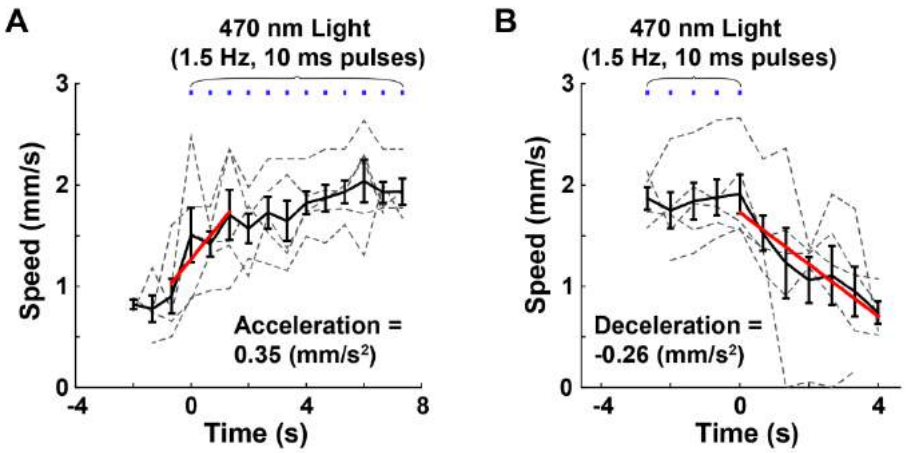

Fig. S11. Acceleration and deceleration when initiating and seizing optical pacing. In less than 5 strokes, tissue-engineered rays reached a stable speed after the initiation of optical pacing (**A**) and tissue-engineered rays decreased the speed by half as soon as the optical pacing was seized (**B**). The speed is calculated by video tracking of the tissue-engineered ray's locomotion in Movie S12. Gray dotted lines and black and red solid lines indicate the individual speed of five tissue-engineered rays, the average speed, and the estimate speed from linear fitting, respectively. Acceleration and deceleration are determined from the slopes of linear fitting of the average speed traces in (**A**) and (**B**), respectively. Error bars indicate standard error of the mean (n=5 rays).

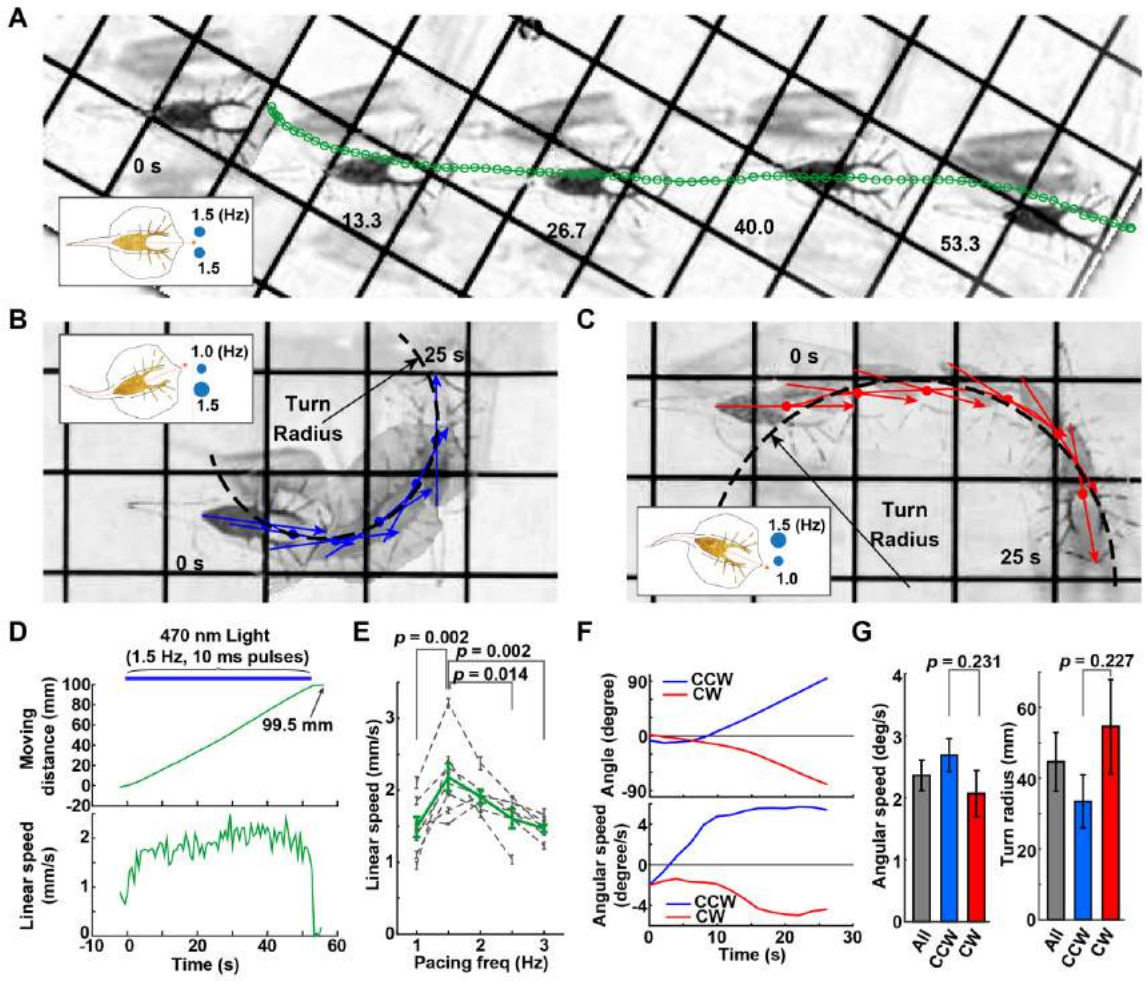

Fig. S12. Frequency-modulated control on swimming speed and direction of tissue-engineered rays. (**A**) Straight, forward locomotion of the tissue-engineered ray by synchronous pacing (1.5 Hz pulses on both fins). Frames from movie S13 at various times showing sustainable and reproducible undulatory locomotion. (**B** and **C**) Counter-clockwise (CCW) and clockwise (CW) turns of the tissue-engineered ray by asynchronous pacing (1.0/1.5 Hz paired pulses). Frames from movie S17 at various times showing that the asynchronous pacing enabled the tissue-engineered ray to change swimming direction by inducing asymmetrical fin motion. (**D**) The undulating motion of fins induced by synchronous pacing enabled the tissue-engineered ray to swim forward over a distance of 99.5 mm with uniform speed. (**E**) Frequency-modulated speed control. Gray and green color indicates the average speed of each tissue-engineered ray during more than 5 strokes, and the average speed of seven tissue-engineered rays, respectively. Tissue-engineered rays had a maximum speed of 1.5-2Hz pacing, and a minimum speed of 1 and 3 Hz. The linear speed at 1.5-2Hz is significantly different from that at 1 and 3 Hz (student t-test: p=0.002, 0.014, and 0.002, respectively). Representative movies are movie S14 to S16. (**F**) For both CCW and CW turns induced by asynchronous pacing, the tissue-engineered ray changed direction up to 90 degrees with increasing angular speed. (**G**) Angular speed and turning radius of the three tissue-engineered rays pacing with

1.0/1.5 or 3.0/1.5 Hz asynchronous pacing. The turning performances are independent of turning direction (For CCW and CW, $p=0.231$ in angular speed $p=0.227$ in turning radius, student t-test, N = 17 turns with 3 tissue-engineered rays).

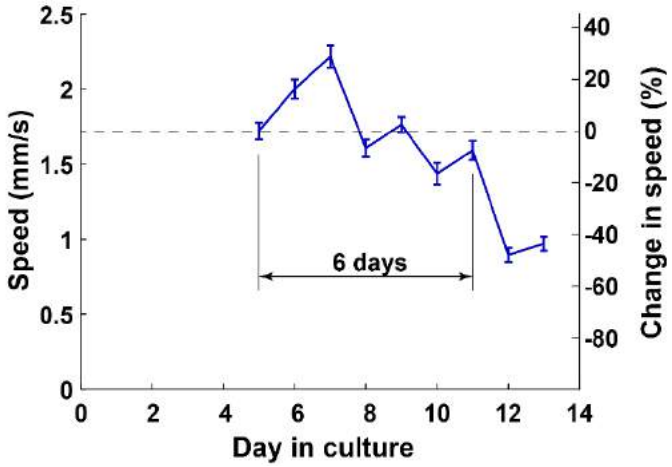

Fig. S13. Durability of a tissue-engineerd ray. The tissue-engineered ray maintained at least 80% of its initial linear speed for up to six days after release, equivalent to a total of 11 days in culture. The tissue-engineered ray was incubated at 37ºC in a supplemented M199 cell media with 2% FBS and transferred in a 37ºC Tyrode's physiological salt solution. Measurements were performed once a day after 5 days in culture. Forward speed was measured while synchronous optical pacing was applied to the anterior part of both fins with 470nm wavelength light and 1.5 Hz frequency, and calculated by video tracking as detailed in the Methods section (sample recordings are reported in Movie S20). Error bars indicate standard error of the mean (n=8-32 strokes).

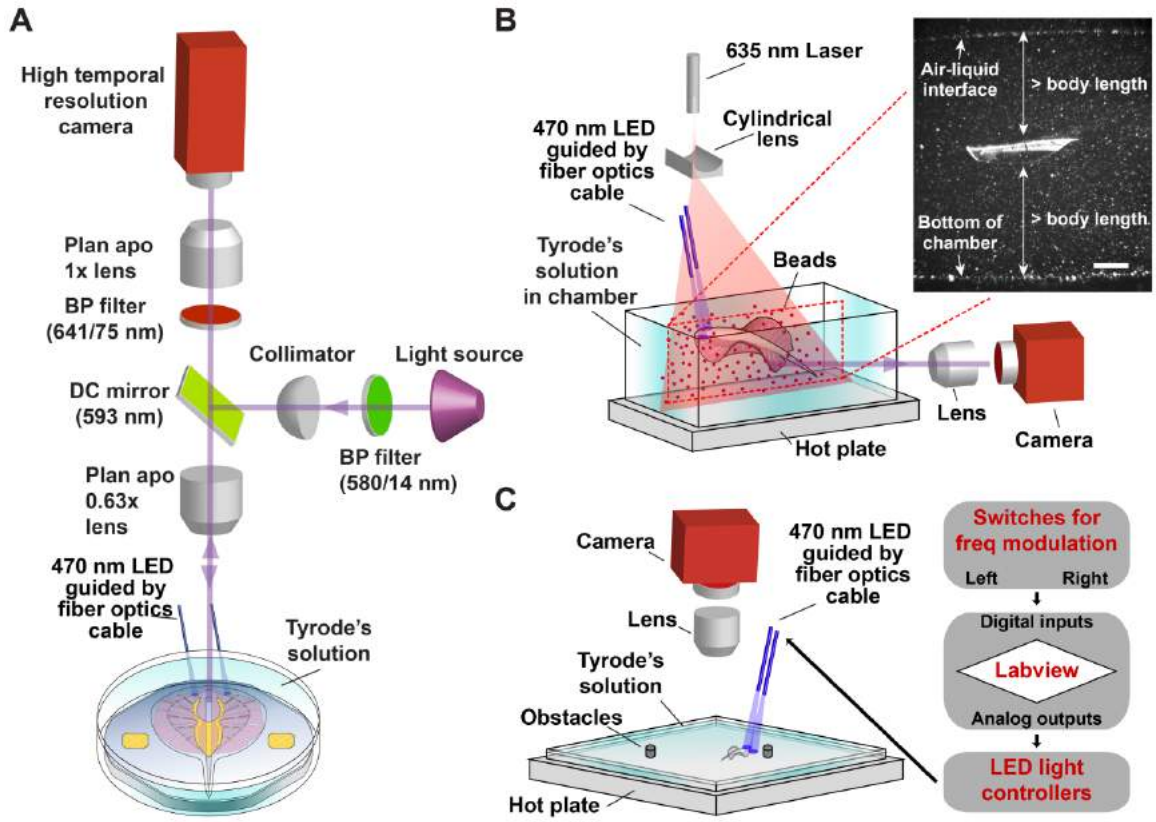

Fig. S14. Experimental setups. (**A**) Optical mapping system for calcium imaging of muscle circuit. To prevent overlay of the excitation light wavelength of calcium transient measurement with excitation of light sensitive ion channels (ChR2 has 380 to 580 nm excitation wavelength in fig. S5G), we used a long wavelength intracellular calcium indicator, X-Rhod-1 (excitation: 574 nm) and a filter set with a wavelength longer than the ChR2 excitation wavelength. We also used a low magnification lens (0.63x, Leica) to expand the field of view to 16 by 16 mm square, which is large enough to see calcium activity over the muscle circuit of the tissue-engineered ray. (**B**) Particle image velocimetry (PIV) setup for imaging fluid movement that the tissue-engineered ray generated with undulatory locomotion. A 635-nm laser was used to prevent overlay of the excitation light wavelength of PIV measurement with excitation of light sensitive ion channels. To minimize the boundary effect from the walls of the chamber and air-liquid interface, we located the tissue-engineered ray in a water chamber with a minimum distance (> the body length of the ray) away from the walls as well as an air-liquid interface to minimize the boundary effect from the walls of the chamber and air-liquid interface. Scale bar, 5 mm. (**C**) Setup for phototactic guidance test. The movement of the tissue-engineered ray was controlled by optical frequency modulation protocols, which were rapidly switched by two push-button operations: the buttons generated digital signals to trigger an LED light controller to switch from synchronous to asynchronous pacing protocols or vice versa through the custom LabVIEW program (National instruments, Austin, TX).

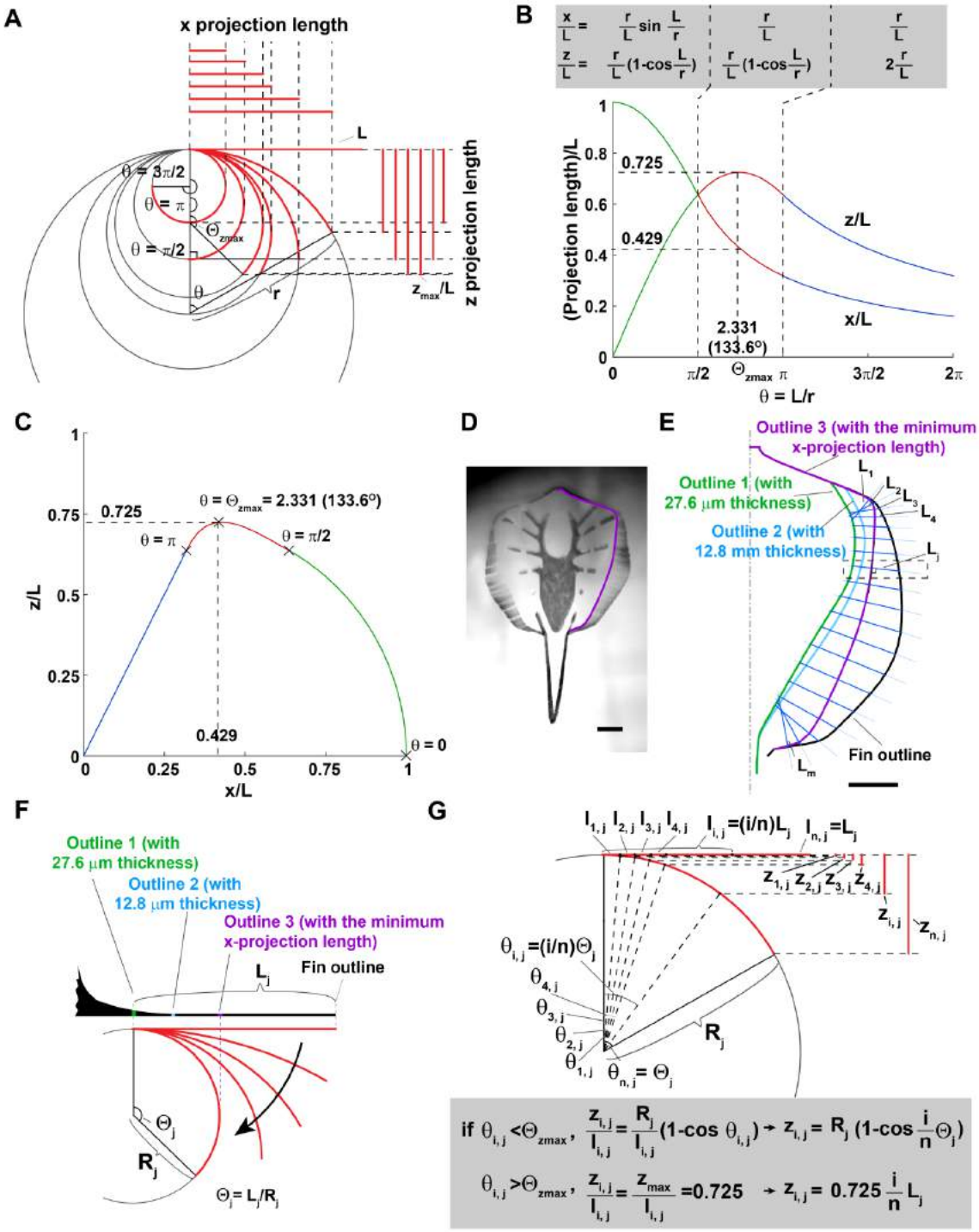

Fig. S15. Structural analysis of fin deflection. (**A** to **C**) Geometric relation of the radius of the curvature (r/L), the angle of the arc ($\theta = L/r$), the x-projection length (x/L), and the z-projection length (z/L) of thin film subject to bending. (**A** and **B**) As thin film is deflected, the radius of the curvature decreases, the angle of the arc increases, the x-projection length decreases, and the z-projection length increases until it reaches the maximum, 0.725, at $\theta = 2.331$, after which it decreases. (**C**) Calculation of the z-projection length from the x-projection length. The maximum z-projection length to

achieve while thin film is deflected from a straight line (θ =0) is calculated from $z/L = r/L(1-\cos(L/r))$ if $\theta \leq 2.331$, but it is 0.725 if $\theta > 2.331$. (**D** to **G**) Calculation of the maximum fin deflection from the outline of minimum *x*-projection length. (**D**) Overlaid frames from Movie S6 to find the outline of minimum *x*-projection length (purple line). Scale bar, 2 mm. (**E**) The tissue-engineered ray fin is assumed to consist of multiple thin films (*j*=1 to *m*) connected in parallel with length, L_j, and oriented in the radial direction of the outline of minimum *x*-projection length (purple). Scale bar, 2 mm. (**F**) The schematics of a transverse section from the mid-disc region of the tissue-engineered ray fin (dashed box in **E**). From distal to proximal, the thickness of the fin is 12.8 μm evenly until the blue outline, after which the thickness dramatically increases up to 500 μm following the height of the body portion of the tissue-engineered ray. The deflection of the body and fin, which are thicker than 27.6 μm (green), is negligible, because the bending modulus of thin film is proportional to the cube of the thickness, and the fin region thicker than 27.6 μm has one order of magnitude higher bending modulus than the 12.8 μm thick fin region. Thus, the length, L_j, of each thin film is calculated from the distance between the fin outline (black) and the outline with 27.6 μm thickness (green). The angle of the arc of *j*th thin film, Θ_j, is calculated with L_j/R_j where R_j is radius of curvature of *j*th thin film. (**G**) Calculation of maximum deflection at multiple points (*i*=1 to *n*) on thin film. The angle of the arc and the length of the thin film at *i*th point on *j*th thin film is calculated with $\theta_{i,j} = (i/n)\,\Theta_j$ and $l_{i,j} = (i/n)\,L_j$, respectively. By considering the relation of the *x*-projection length and the maximum fin deflection (**C**), the maximum deflection at *i*th point on *j*th thin film is calculated with $z_{i,j} = R_j(1- \cos((i/n)\Theta_j))$, if $\theta_{i,j} \leq 2.331$ and $z_{i,j} = 0.725(i/n)L_j$, if $\theta_{i,j} > 2.331$. Using this structural analysis, we calculated the maximum deflection pattern of the tissue-engineered ray (Fig. 3I) from the outline of the minimum *x*-projection length (**D**).

Movie S1: Undulatory locomotion of a Little skate
Lateral view movie of a Little skate, *L. erinacea*, swimming freely in a recirculating flow tank at a speed of 2.0 body lengths per second (~ 15 cm/s). High-speed video at 250 Hz revealed the motion of the wing and lateral view videos like this one are synchronized with dorsal view videos to allow three-dimensional reconstruction of wing motion. Scale bar, 2 cm.

Movie S2: Micro-CT scan of three dimensional structure of the tissue-engineered ray
The micro-CT scan data was reconstructed along horizontal (middle), sagittal (right) and coronal (top) planes. The tissue-engineered ray has a three-dimensional structure of the dorsoventral disk, showing decreasing thicknesses from proximal to distal and from anterior to posterior. Red and blue lines indicate the locations of displayed sagittal and coronal planes, respectively, among the horizontal plane. Scale bars, 2 mm (horizontal plane) and 0.5 mm (sagittal and coronal plane).

Movie S3: Calcium propagation in muscle circuit with the serpentine pattern of choice
The muscle circuit was fabricated by culturing rat cardiac cells on the fibronection (FN)-patterned elastomer substrate. The calcium propagation in the muscle circuit was monitored with a calcium indicator, X-Rhod-1. The synchronous optical pacing was applied at the anterior part of muscle circuits in both fins using a light source of 470nm wavelength with frequencies of 1, 1.5, 2, 2.5, and 3 Hz. The muscle circuit with the serpentine pattern of choice was designed to have 10 parallel sections of serpentine patterns on each fin. Parallel sections were separated by gaps at least 100 μm wide in order to prevent cardiac cells from spanning over the adjacent parallel sections. Calcium waves initiated by local optical stimulation at the anterior part propagated through the serpentine pattern along anterior-posterior axis. The movie is playing 5× slower. Scale bar, 2 mm.

Movie S4: Calcium propagation of the muscle circuits without serpentine pattern and with a dense serpentine pattern
Muscle circuits with different serpentine patterns were designed to compare calcium propagation with the serpentine pattern of choice (10 parallel sections, movie S3); one without the serpentine pattern (top) and the other with a dense serpentine pattern having 20 parallel sections (bottom). The calcium propagation of both muscle circuits was monitored with a calcium indicator, X-Rhod-1, and the synchronous optical pacing was applied at the anterior part of both fins with 470nm wavelength light and 1.5, 2, and 3 Hz frequencies. The calcium imaging shows that the number of waves present in the fins is controllable by varying pacing frequency or serpentine pattern density (number of parallel section serpentine patterns per given fin area). The movie is playing 5× slower. Scale bar, 2 mm.

Movie S5: Asynchronous optical pacing for muscle circuit
The muscle circuit with the serpentine pattern of choice was calcium-imaged with a calcium indicator, X-Rhod-1, while the anterior part of the muscle circuits on both sides

were paced asynchronously with paired frequencies of 1/1.5 Hz (top) and 3/1.5 (bottom). The individual muscle circuits can be controlled independently by asynchronous pacing. The movie is playing 5× slower. Scale bar, 2 mm.

Movie S6: Undulatory locomotion of the tissue-engineered ray paced at 1.5 Hz
The undulatory locomotion of the tissue-engineered ray in Tyrode's solution was recorded at 100 frames per second. The synchronous optical pacing at 1.5 Hz frequency was applied at the anterior part of both fins. The tissue-engineered ray swims with undulating motion of both fins in a rhythmic fashion following the optical pacing. The muscle contraction was initiated at the anterior of both fins and the muscular wave propagated from anterior to posterior. The tissue-engineered ray showed slower forward locomotion when the wave was propagating, after which it moved at its maximum speed when the wave reached the posterior part of the fin. In addition, the tissue-engineered ray displayed an asymmetric deflection pattern as the batoid fish show: deflection amplitude of fins increased until mid-disc and then remained constant through anterior-posterior axis, while amplitude increases across mediolateral fin axes. The movie is playing 5× slower. Scale bar, 2 mm.

Movie S7: Comparison between undulation by point pacing and pulsatile propulsion by field pacing
The locomotion of the same tissue-engineered ray was compared when two different stimulation methods were applied: the optical point stimulation was applied at the anterior part of both fins with 400-μm optical fibers, while the electrical field stimulation was applied to the entire muscle tissue of both fins by placing the ray between two 8 cm separated platinum electrodes. Both optical stimulation frequencies are 1.5 Hz. The optical point stimulation induced sequential muscle activation, generating undulation, while the electrical field stimulation induced global contraction of both fins, generating pulsatile propulsion. The optical point stimulation improved the swimming speed compared with the electrical field stimulation. The movie is playing in real-time. Grid, 1 cm.

Movie S8: Locomotion of the tissue-engineered ray with symmetrical body
To evaluate the effect of an asymmetrical body shape on swimming efficiency, the tissue-engineered ray with the symmetrical body was designed as a control. The fin deflection of the tissue-engineered ray with the symmetrical body was significantly greater than that of the ray with the asymmetrical body (movie S6). As a consequence, the symmetrical tissue-engineered ray's speed was reduced, compared to the asymmetrical tissue-engineered ray (movie S6). The optical stimulation frequency was 1.5 Hz. The movie is playing in real-time. Scale bar, 1 cm.

Movie S9: Locomotion of the tissue-engineered ray with various structural designs
To evaluate the effect of gold skeleton and fin structures on swimming efficiency, the tissue-engineered rays without a gold skeleton (top left, 1Hz pacing), with a denser gold skeleton (top right, 2Hz pacing), and with thicker (bottom left, 2Hz pacing) and thinner (bottom right, 1Hz pacing) fins were designed as controls. The swimming speed of these tissue-engineered rays decreased dramatically. The thinner fins (9.18 μm) deflected with

large amplitude because of the decreased stiffness of the substrate. When the deflection amplitude exceeds a critical value, the benefit of the displacing larger masses of fluid is counterbalanced and dominated by the increased drag associated with a larger effective frontal area, thus impairing forward speed. The movie is playing in real-time. Scale bar and grid, 1 cm.

Movie S10: Fluid motion of the tissue-engineered ray generated by undulatory locomotion
The fluid motion generated by undulatory locomotion of the tissue-engineered ray was recorded with a particle image velocimetry (PIV) method at 100 frames per second. The synchronous optical pacing at 1.5 Hz frequency is applied at the anterior part of both fins. Silver coated hollow glass microspheres with 5-15 μm diameters and neutral buoyancy (1.08 g/mm density) were used to enhance the intensity of reflected light, but affected the viability of cardiac cells showing weak contraction. The PIV data shows that the undulating motion of the fins produced alternated positive and negative vortices. The movie is playing 5× slower. Scale bar, 2 mm.

Movie S11: Fluid motion of the Little skate generated by undulatory locomotion
Lateral view movie of a Little skate, *L. erinacea*, swimming freely in a laser light sheet within a recirculating flow tank at a speed of 2.0 body lengths per second (~ 15 cm/s). A continuous wave laser was used to illuminate particles in the flow and reveal body and wake flow patterns during locomotion. Scale bar, 2 cm.

Movie S12: Acceleration and deceleration of the tissue-engineered ray induced by optical stimulation
The change in thrust was monitored when initiating (right) and seizing (left) the synchronous pacing with 1.5 Hz frequency. As soon as we optically stimulated the tissue-engineered rays that were initially moving in uncoordinated spontaneous motions, they reached a stable swimming speed with coordinated motion within 5 strokes. As soon as the stimulation was seized, the tissue-engineered rays stopped or decreased their speed with uncoordinated spontaneous motions. The movie is playing in real-time. Grid, 1 cm.

Movie S13: Sustainable directional locomotion with synchronous pacing
The directional locomotion of the tissue-engineered ray was monitored while synchronous optical pacing was applied at the anterior part of both fins. The synchronous pacing induced a coordinated undulating motion of the fins and generated unidirectional locomotion (99.5 mm moving distance) with stable cruising speed. The movie is playing in real-time. Grid, 1 cm.

Movie S14: Undulation with various pacing frequency (slow motion video)
The tissue-engineered ray was stimulated with synchronous optical pacing with varying pacing frequencies (1, 1.5, 2, 2.5 and 3 Hz). The locomotion of the tissue-engineered ray was recorded at 100 frames per second. The swimming speed of the tissue-engineered ray reached the maximum and minimum at the frequencies of 2 Hz and 1 Hz, respectively. The red line indicates the initial position of the tissue-engineered ray. The movie is playing 5× slower. Scale bar, 2 mm.

Movie S15: Undulation with various pacing frequencies (video from a 45 degree angle view toward the dorsal of the fins)
The tissue-engineered ray was stimulated with synchronous optical pacing with varying pacing frequencies (1.5, 2 and 3 Hz). The locomotion of the ray was recorded from a 45-degree angle view toward the dorsal of the fins, to monitor the propagation of wave best. The swimming speed of this tissue-engineered ray reached the minimum and maximum speed at frequencies of 3 Hz and 2 Hz, respectively. The movie is playing in real-time. Grid, 1 cm.

Movie S16: Undulation with various pacing frequencies (video from dorsal view)
The tissue-engineered ray was stimulated with synchronous optical pacing with varying pacing frequencies (1, 1.5, 2 and 3 Hz). The locomotion of the ray was recorded from the dorsal view. This tissue-engineered ray reached the minimum and maximum speed at frequencies of 1 Hz and 1.5 Hz, respectively. The maximum speed is 3.2 mm/s. The movie is playing in real-time. Grid, 1 cm.

Movie S17: Counterclockwise and clockwise turns with asynchronous pacing (1.5/1 Hz)
The counterclockwise and clockwise turns of the tissue-engineered ray were monitored while it was asynchronously paced with pairing frequencies (1.5 Hz and 1 Hz). The 1.5 Hz pacing generated faster locomotion than the 1Hz pacing, so the ray turned to 1Hz pacing direction. The movie is playing 2× faster. Grid, 1 cm.

Movie S18: Counterclockwise turn with asynchronous pacing (1.5/3 Hz)
The counterclockwise turn of the tissue-engineered ray was monitored while it was asynchronously paced with pairing frequencies (1.5 Hz and 3 Hz). The 1.5 Hz pacing applied on the left fin generated faster locomotion than the 3Hz pacing applied on the right fin, so the ray turned counterclockwise. The movie is playing 2× faster. Grid, 1 cm.

Movie S19: Phototactic guidance of tissue-engineered ray
The obstacle course was designed to challenge maneuverability of the tissue-engineered ray. The three obstacles were placed with 7.5 cm distance which was longer than the average turning radius of the tissue-engineered ray, 4.5 cm. The direction of the tissue-engineered ray was controlled by combinational pacing protocols (synchronous: 1.5 Hz on both fins and asynchronous pacing: paired 1.5 and 3 Hz), which were rapidly manipulated by digital trigger signals to an LED light controller through the custom LabVIEW program (fig. S14C). The tissue-engineered ray completed the obstacle course by generating counterclockwise and clockwise turns as well as directional locomotion. The movie is playing 5× faster. Grid, 1 cm.

Movie S20: Durability measurements of a tissue-engineered ray
The locomotion of the tissue-engineered ray was monitored for 8 days. After 5 days in culture, the ray was released (top left). The swimming speed was found to increase during two days (a total of 7 days in culture, top right), to then stabilize within 80% of initial speed for up to six days (a total of 11 days in culture, bottom left). After this time,

substantial performance degradation was observed (a total of 13 days in culture, bottom right). The locomotion of the tissue-engineered ray was recorded at 60 frames per second while the ray was stimulated with synchronous optical pacing at 1.5 Hz frequency. The movie plays in real-time. Grid, 1 cm.

References and Notes

1. W. G. Bearcroft, Zika virus infection experimentally induced in a human volunteer. *Trans. R. Soc. Trop. Med. Hyg.* **50**, 442–448 (1956). Medline doi:10.1016/0035-9203(56)90090-6

2. V. M. Cao-Lormeau, A. Blake, S. Mons, S. Lastère, C. Roche, J. Vanhomwegen, T. Dub, L. Baudouin, A. Teissier, P. Larre, A. L. Vial, C. Decam, V. Choumet, S. K. Halstead, H. J. Willison, L. Musset, J. C. Manuguerra, P. Despres, E. Fournier, H. P. Mallet, D. Musso, A. Fontanet, J. Neil, F. Ghawché, Guillain-Barré Syndrome outbreak associated with Zika virus infection in French Polynesia: A case-control study. *Lancet* **387**, 1531–1539 (2016). Medline doi:10.1016/S0140-6736(16)00562-6

3. S. A. Rasmussen, D. J. Jamieson, M. A. Honein, L. R. Petersen, Zika virus and birth defects—Reviewing the evidence for causality. *N. Engl. J. Med.* **374**, 1981–1987 (2016). Medline doi:10.1056/NEJMsr1604338

4. D. L. Heymann, A. Hodgson, A. A. Sall, D. O. Freedman, J. E. Staples, F. Althabe, K. Baruah, G. Mahmud, N. Kandun, P. F. Vasconcelos, S. Bino, K. U. Menon, Zika virus and microcephaly: Why is this situation a PHEIC? *Lancet* **387**, 719–721 (2016). Medline doi:10.1016/S0140-6736(16)00320-2

5. D. Leung, K. Schroder, H. White, N. X. Fang, M. J. Stoermer, G. Abbenante, J. L. Martin, P. R. Young, D. P. Fairlie, Activity of recombinant dengue 2 virus NS3 protease in the presence of a truncated NS2B co-factor, small peptide substrates, and inhibitors. *J. Biol. Chem.* **276**, 45762–45771 (2001). Medline doi:10.1074/jbc.M107360200

6. P. Erbel, N. Schiering, A. D'Arcy, M. Renatus, M. Kroemer, S. P. Lim, Z. Yin, T. H. Keller, S. G. Vasudevan, U. Hommel, Structural basis for the activation of flaviviral NS3 proteases from dengue and West Nile virus. *Nat. Struct. Mol. Biol.* **13**, 372–373 (2006). Medline doi:10.1038/nsmb1073

7. D. Luo, S. G. Vasudevan, J. Lescar, The flavivirus NS2B-NS3 protease-helicase as a target for antiviral drug development. *Antiviral Res.* **118**, 148–158 (2015). Medline doi:10.1016/j.antiviral.2015.03.014

8. N. R. Faria, R. S. Azevedo, M. U. Kraemer, R. Souza, M. S. Cunha, S. C. Hill, J. Thézé, M. B. Bonsall, T. A. Bowden, I. Rissanen, I. M. Rocco, J. S. Nogueira, A. Y. Maeda, F. G. Vasami, F. L. Macedo, A. Suzuki, S. G. Rodrigues, A. C. Cruz, B. T. Nunes, D. B. Medeiros, D. S. Rodrigues, A. L. Nunes Queiroz, E. V. da Silva, D. F. Henriques, E. S. Travassos da Rosa, C. S. de Oliveira, L. C. Martins, H. B. Vasconcelos, L. M. Casseb, D. B. Simith, J. P. Messina, L. Abade, J. Lourenço, L. Carlos Junior Alcantara, M. M. de Lima, M. Giovanetti, S. I. Hay, R. S. de Oliveira, P. S. Lemos, L. F. de Oliveira, C. P. de Lima, S. P. da Silva, J. M. de Vasconcelos, L. Franco, J. F. Cardoso, J. L. Vianez-Júnior, D. Mir, G. Bello, E. Delatorre, K. Khan, M. Creatore, G. E. Coelho, W. K. de Oliveira, R. Tesh, O. G. Pybus, M. R. Nunes, P. F. Vasconcelos, Zika virus in the Americas: Early epidemiological and genetic findings. *Science* **352**, 345–349 (2016). Medline doi:10.1126/science.aaf5036

9. C. G. Noble, C. C. Seh, A. T. Chao, P. Y. Shi, Ligand-bound structures of the dengue virus protease reveal the active conformation. *J. Virol.* **86**, 438–446 (2012). Medline doi:10.1128/JVI.06225-11

10. L. Türker, Some boric acid esters of glycerol – An *ab initio* treatment. *Indian J. Chem.* **45A**, 1339–1344 (2006).

11. S. Aguirre, A. M. Maestre, S. Pagni, J. R. Patel, T. Savage, D. Gutman, K. Maringer, D. Bernal-Rubio, R. S. Shabman, V. Simon, J. R. Rodriguez-Madoz, L. C. Mulder, G. N. Barber, A. Fernandez-Sesma, DENV inhibits type I IFN production in infected cells by cleaving human STING. *PLOS Pathog.* **8**, e1002934 (2012). Medline doi:10.1371/journal.ppat.1002934

12. R. Hamel, O. Dejarnac, S. Wichit, P. Ekchariyawat, A. Neyret, N. Luplertlop, M. Perera-Lecoin, P. Surasombatpattana, L. Talignani, F. Thomas, V. M. Cao-Lormeau, V. Choumet, L. Briant, P. Desprès, A. Amara, H. Yssel, D. Missé, Biology of Zika virus infection in human skin cells. *J. Virol.* **89**, 8880–8896 (2015). Medline doi:10.1128/JVI.00354-15

13. M. C. Lawrence, P. M. Colman, Shape complementarity at protein/protein interfaces. *J. Mol. Biol.* **234**, 946–950 (1993). Medline doi:10.1006/jmbi.1993.1648

14. D. Kuroda, J. J. Gray, Shape complementarity and hydrogen bond preferences in protein-protein interfaces: Implications for antibody modeling and protein-protein docking. *Bioinformatics* btw197 (2016). 10.1093/bioinformatics/btw197 Medline doi:10.1093/bioinformatics/btw197

15. P. G. Richardson, P. Sonneveld, M. W. Schuster, D. Irwin, E. A. Stadtmauer, T. Facon, J. L. Harousseau, D. Ben-Yehuda, S. Lonial, H. Goldschmidt, D. Reece, J. F. San-Miguel, J. Bladé, M. Boccadoro, J. Cavenagh, W. S. Dalton, A. L. Boral, D. L. Esseltine, J. B. Porter, D. Schenkein, K. C. Anderson; Assessment of Proteasome Inhibition for Extending Remissions (APEX) Investigators, Bortezomib or high-dose dexamethasone for relapsed multiple myeloma. *N. Engl. J. Med.* **352**, 2487–2498 (2005). Medline doi:10.1056/NEJMoa043445

16. Z. Yin, S. J. Patel, W. L. Wang, G. Wang, W. L. Chan, K. R. R. Rao, J. Alam, D. A. Jeyaraj, X. Ngew, V. Patel, D. Beer, S. P. Lim, S. G. Vasudevan, T. H. Keller, Peptide inhibitors of Dengue virus NS3 protease. Part 1: Warhead. *Bioorg. Med. Chem. Lett.* **16**, 36–39 (2006). Medline doi:10.1016/j.bmcl.2005.09.062

17. M. Z. Hammamy, C. Haase, M. Hammami, R. Hilgenfeld, T. Steinmetzer, Development and characterization of new peptidomimetic inhibitors of the West Nile virus NS2B-NS3 protease. *ChemMedChem* **8**, 231–241 (2013). Medline doi:10.1002/cmdc.201200497

18. T. G. Battye, L. Kontogiannis, O. Johnson, H. R. Powell, A. G. Leslie, *iMOSFLM*: A new graphical interface for diffraction-image processing with *MOSFLM*. *Acta Crystallogr. D Biol. Crystallogr.* **67**, 271–281 (2011). Medline doi:10.1107/S0907444910048675

19. P. R. Evans, An introduction to data reduction: Space-group determination, scaling and intensity statistics. *Acta Crystallogr. D Biol. Crystallogr.* **67**, 282–292 (2011). Medline doi:10.1107/S090744491003982X

20. P. D. Adams, P. V. Afonine, G. Bunkóczi, V. B. Chen, I. W. Davis, N. Echols, J. J. Headd, L. W. Hung, G. J. Kapral, R. W. Grosse-Kunstleve, A. J. McCoy, N. W. Moriarty, R. Oeffner, R. J. Read, D. C. Richardson, J. S. Richardson, T. C. Terwilliger, P. H. Zwart, *PHENIX*: A comprehensive Python-based system for macromolecular structure solution.

Acta Crystallogr. D Biol. Crystallogr. **66**, 213–221 (2010). Medline doi:10.1107/S0907444909052925

21. L. Jaroszewski, Z. Li, X. H. Cai, C. Weber, A. Godzik, FFAS server: Novel features and applications. *Nucleic Acids Res.* **39** (suppl), W38–W44 (2011). Medline doi:10.1093/nar/gkr441

22. G. N. Murshudov, A. A. Vagin, E. J. Dodson, Refinement of macromolecular structures by the maximum-likelihood method. *Acta Crystallogr. D Biol. Crystallogr.* **53**, 240–255 (1997). Medline doi:10.1107/S0907444996012255

23. P. Emsley, B. Lohkamp, W. G. Scott, K. Cowtan, Features and development of *Coot*. *Acta Crystallogr. D Biol. Crystallogr.* **66**, 486–501 (2010). Medline doi:10.1107/S0907444910007493

24. P. Gouet, E. Courcelle, D. I. Stuart, F. Métoz, ESPript: Analysis of multiple sequence alignments in PostScript. *Bioinformatics* **15**, 305–308 (1999). Medline doi:10.1093/bioinformatics/15.4.305

25. U. W. Arndt, R. A. Crowther, J. F. Mallett, A computer-linked cathode-ray tube microdensitometer for x-ray crystallography. *J. Sci. Instrum.* **1**, 510–516 (1968). Medline doi:10.1088/0022-3735/1/5/303

26. M. S. Weiss, R. Hilgenfeld, On the use of the merging *R* factor as a quality indicator for X-ray data. *J. Appl. Cryst.* **30**, 203–205 (1997). doi:10.1107/S0021889897003907

27. P. A. Karplus, K. Diederichs, Linking crystallographic model and data quality. *Science* **336**, 1030–1033 (2012). Medline doi:10.1126/science.1218231

28. V. B. Chen, W. B. Arendall 3rd, J. J. Headd, D. A. Keedy, R. M. Immormino, G. J. Kapral, L. W. Murray, J. S. Richardson, D. C. Richardson, *MolProbity*: All-atom structure validation for macromolecular crystallography. *Acta Crystallogr. D Biol. Crystallogr.* **66**, 12–21 (2010). Medline doi:10.1107/S0907444909042073